PRECAMBRIAN RESEARCH

Petrology and geochemistry of the ~2.9 Ga Itilliarsuk banded iron formation and associated supracrustal rocks, West Greenland: Source characteristics and depositional environment

Rasmus Haugaard [a,b,c,*], Robert Frei [a,b], Henrik Stendal [d,1], Kurt Konhauser [c]

[a] Geological Institute, University of Copenhagen, Øster Voldgade 10, DK-1350 Copenhagen K, Denmark
[b] Nordic Center for Earth Evolution, NordCEE, Denmark
[c] Department of Earth and Atmospheric Sciences, University of Alberta, Edmonton, Alberta, T6G 2E3, Canada
[d] Geological Survey of Denmark and Greenland, Øster Voldgade 10, DK-1350 Copenhagen K, Denmark

ARTICLE INFO

ABSTRACT

Here we present new field, petrographic and geochemical data from the ~2.9 Ga Itilliarsuk banded iron formation (BIF) and associated lithologies within the Itilliarsuk supracrustal belt, south-eastern Nussuuaq, West Greenland. The supracrustals represent a volcanic–sedimentary sequence, which rests unconformably on a basement of tonalite–trondhjemite–granodiorite (TTG) lithologies. Felsic meta-greywackes, meta-semipelites and thinly bedded ferruginous shales were identified intercalated with the Itilliarsuk BIF. Other associated rocks include metapelites, acidic metavolcanics and metagabbroic sills. The supracrustals have experienced amphibolite-facies metamorphism, which has resulted in complete resetting of the U–Pb system with an apparent age of 1895 ± 48 Ma. This tectono-metamorphic event corresponds well with the Paleoproterozoic Rinkian orogeny known from this region. The Itilliarsuk-(oxide-facies) BIF has been divided into two segments on the basis of major and trace elements chemistry: a shaley-BIF with a strong clastic component and a more chemically pure BIF. The shaley-BIF contains high terrigenous influx as reflected by elevated Al_2O_3 (up to 12 wt.%), TiO_2, high field strength elements (HFSE) and transition metals. The chemically pure BIF is characterised by alternating high iron (~68 wt.%) and high silica (~64 wt.%) bands with low total rare earths and yttrium (REY), Al_2O_3, TiO_2 and HFSE contents, suggesting a low detrital component. The least altered bands of the BIF record diagnostic Archaean seawater features with Post-Archaean Average Shale (PAAS)-normalised positive La- and Eu-anomalies, enrichment in heavy rare earth elements (HREE) relative to light rare earth elements (LREE) [$(Pr/Yb)_{PAAS} < 1$], and absence of Ce-anomalies which suggests deposition from an anoxic water column. Sm–Nd isotopes of the chemically pure silica-rich bands record T_{DM} model ages of 3.23–2.85 Ga and initial ε_{Nd} ($\varepsilon_{Nd}(i)$) values in the range of +0.43 to +4.05, average of +1.35. In contrast, the chemically pure Fe-rich bands yield T_{DM} model ages of 3.61–3.22 Ga and $\varepsilon_{Nd}(i)$ values from −2.87 to +0.09, average of −1.29. The associated supracrustal rocks in the study area have significantly higher, positive $\varepsilon_{Nd}(i)$ values. The $^{143}Nd/^{144}Nd$ in the Itilliarsuk BIF, therefore, contrasts world BIFs by exhibiting radiogenic, positive $\varepsilon_{Nd}(i)$ values in shallow seawaters where the REY's were controlled by a local, depleted continental crust, whereas the negative $\varepsilon_{Nd}(i)$ values found in the iron-rich layers suggest that the submarine hydrothermal source was influenced by an enriched mantle, possibly an older subcontinental lithospheric segment. The felsic metagreywackes are immature, first-cycle ($SiO_2/Al_2O_3 \sim 4.4$, $[La/Yb \gg 1]_{CHON}$) metasediments with affinities to TTG-suites, primarily extrusives, whereas the meta-semipelites and metapelites contain a larger mafic contribution with higher content of Fe_2O_3, MgO, Cr, Ni and HREEs. This suggests that the BIF was deposited in a highly unstable basin, presumably in a palaeo-continental slope or outer shelf environment, with frequent fluctuations of epiclastic and volcanogenic sediments derived from adjacent bimodal sources. The T_{DM} model ages and the use of Th–Sc–Zr and La–Th–Sc tectonic discrimination plots indicate that the metasediments were sourced from a juvenile ocean island arc setting.

© 2012 Elsevier B.V. All rights reserved.

* Corresponding author at: Department of Earth and Atmospheric Sciences, University of Alberta, Edmonton, Alberta, Canada T6G 2E3. Tel.: +1 780 492 6532; fax: +1 780 492 2030.
  E-mail addresses: rasmus@ualberta.ca, rebstrup@hotmail.com (R. Haugaard).
[1] Present address: Bureau of Minerals and Petroleum, Imaneq 29, P.O. Box 930, 3900 Nuuk, 9 Greenland.

1. Introduction

Banded iron formations (BIFs) are chemical sediments that precipitated throughout the Archaean and early Paleoproterozoic. The majority of BIFs consist of alternating silica-rich and iron-rich bands that range from small-scale laminated microbands (few mm), through mesobands (≥ 10 mm) and up to metre-scale macrobands (Trendall and Blockley, 2004). The mineral composition of BIF has been modified by diagenetic and metamorphic overprinting, and therefore, the main mineral phases now found in BIF, such as hematite (Fe_2O_3), magnetite (Fe_3O_4), microcrystalline quartz (SiO_2), stilpnomelane ($K(Fe,Mg)_8(Si,Al)_{12}(O,OH)_{27}$), Fe-amphiboles, calcite and dolomite-ankerite are actually of secondary origin. Proposed primary minerals are ferric hydroxide ($Fe(OH)_3$), siderite ($FeCO_3$), greenalite (($Fe)_3Si_2O_5(OH)_4$) and amorphous silica (Klein, 2005). The bulk of the iron in BIF originated as dissolved Fe(II) from submarine hydrothermal vents and was subsequently transformed to dissolve Fe(III) in the upper water column by either abiological or biological oxidation. The ferric iron then hydrolysed rapidly to ferric hydroxide and settled to the sea floor where further transformations ensued (Bekker et al., 2010). Silica was either sourced from hydrothermal venting (Steinhöfel et al., 2010) or from continental weathering (Hamade et al., 2003).

As marine chemical sediments, the trace element and isotopic composition of BIF have been used as proxies for understanding Earth's ancient surface environment. In particular, several recent studies have used BIF to constrain the preceding period of arguably the most important transition in Earth's history, that being the 'Great Oxidation Event' (GOE) at around 2.5 billion years ago when the atmosphere became oxygenated. For instance, temporal trends in BIF Ni content have led to the suggestion that the oceans before 2.7 Ga could have supported the growth of methane-producing bacteria throughout much of the water column, but a significant decline in seawater Ni concentrations thereafter led to a methanogen Ni-famine, a subsequent drop in methane production, and ultimately a rise in atmospheric O_2 as oxygen-producing cyanobacteria expanded deeper into the water column left vacant by the methanogens (Konhauser et al., 2009). Based on Cr isotope values in BIF through time, Frei et al. (2009) found that cyanobacterial activity may already have been abundant by 2.8 Ga ago, and that their production of O_2 may have led to Earth's first oxidative weathering of the continents several hundred millions years earlier than the GOE. Supporting evidence for oxygenated marine surface waters between 2.8 and 2.7 Ga comes from ^{13}C enrichment in kerogens (Eigenbrode and Freeman, 2006), cyanobacterial and methanotrophic biomarkers in shales and carbonates (Eigenbrode et al., 2008), high Re concentrations in black shales (Kendall et al., 2010) and N isotopic values in kerogens indicative of a coupled nitrification–denitrification cycle (Godfrey and Falkowski, 2009). However, relative to the GOE, the oxidative weathering during the Mesoarchaean may not have been very profound as suggested by generally lower authigenic Cr supply to the oceans (Konhauser et al., 2011).

As the timing for the spread of cyanobacteria, and the oxidation of the surface environment, is being pushed back in time, it becomes critical to analyse BIF from strata older than 2.8 Ga to assess the composition of seawater and the impact of continental weathering vs. submarine hydrothermal fluids on the source of solutes, and ultimately the diversity of the marine biosphere at that time. Previous work attempting to ascertain the composition of Mesoarchaean (3.2–2.8 Ga) oceans has focused on rare earth element and yttrium (REY) patterns of individual bands within BIF. With few exceptions, Post-Archaean Average Shale (PAAS)-normalised REY patterns of BIF are similar to those of modern seawater, exhibiting low REY contents, positive La- and Y-anomalies and depletion of light rare earth elements (LREEs) relative to heavy rare earth elements

(HREEs) (Bau and Dulski, 1996; Bolhar et al., 2004; Johannesson et al., 2006). The exceptions are that Archaean BIFs have positive Eu-anomalies and they do not show the characteristic strongly negative Ce-anomalies of modern seawater. The former is attributed to high-temperature (>250 °C) hydrothermal fluids from mid-ocean ridges and back-arc spreading zones injecting solutes into anoxic bottom waters (Bau and Möller, 1993), while the latter reflects the lack of significant oxidizing agents (e.g. O_2) to fractionate Ce(III) from neighbouring REEs (Bolhar et al., 2004; Rollinson, 2007). Neodymium (Nd) isotopes have also shown to be highly valuable in tracing the continental vs. hydrothermal input to BIF. For example, the 2.9 Ga Nemo BIF in North America records mixing of $^{143}Nd/^{144}Nd$ from primarily two sources: (1) anoxic deep water with generally positive initial ε_{Nd} ($\varepsilon_{Nd}(i)$) values, reflecting submarine MORB-like depleted sources, and (2) shallower waters with generally lower $\varepsilon_{Nd}(i)$, reflecting riverine input from evolved continental sources (Frei et al., 2008). Newly compiled $^{143}Nd/^{144}Nd$ data by Alexander et al. (2009) of BIF older than 2.7 Ga suggests that bulk anoxic Archaean seawater was dominated by high-temperature hydrothermal alteration of mantle-derived oceanic crust, presumably also responsible for delivering the iron to the BIF. However, deviation from this mantle Nd signal has been recorded in the 2.9 Ga Pongola BIF in South Africa which was deposited in a near-shore, shallow-water environment where continental fluxes of Fe and other solutes contributed greatly to the unit's composition (Alexander et al., 2009).

Despite the previous studies on Mesoarchean BIF that have focused on the source of the BIF components, there is a paucity of information pertaining to the trace element composition of those BIF, and in particular, what they might tell us about ancient seawater chemistry. In this regard, we have investigated the composition of the relatively unexplored Itilliarsuk BIF exposed within the Mesoarchaean Itilliarsuk supracrustal belt on south-eastern Nuussuaq, West Greenland. Major and trace elements whole-rock geochemical analyses, as well as Nd and Pb isotope analyses have been carried out on individual micro- and mesobands from the BIF and associated lithologies. In addition to the BIF, the interbedded clastic metasediments have also been analysed in order to draw an interpretation of the depositional environment of the Itilliarsuk BIF. We show here that the BIF was deposited in an anoxic water column, with no evidence for surface water oxygenation, and by extension, abundant cyanobacterial activity.

2. Geological background

The Itilliarsuk BIF is exposed in the promontory called the Itilliarsuup Qaqqaa (Fig. 1). The area comprises the western part of a 25 km, ENE–WSW trending belt of Archean supracrustals called the Itilliarsuk supracrustal rocks. The belt belongs to the southern part of the Nuussuaq domain and is located along the northern shore of the Torsukattat ice-fjord, on the south-east Nuussuaq (Fig. 1). With a total of 2.5 km, the Itilliarsuup Qaqqaa is the thickest sequence in the Itilliarsuk supracrustals (Garde and Steenfelt, 1999). Presented in Fig. 2A is a field photo with an overview of Itilliarsuup Qaqqaa and the main lithologies; the main lithologies are placed into the general stratigraphical column in Fig. 2B.

The main structural defomation and the metamorphic overprinting of the Nuussuaq domain developed primarily during the early Proterozoic Rinkian orogenic event, ca. 1.7–1.8 Ga ago (Garde and Steenfelt, 1999). A SSE-dipping Palaeoproterozoic shear zone along the Torsukattak ice-fjord divides the Nuussuaq domain from the southern Ataa domain. Evidence from the acidic metavolcanic unit at the southern part of Itilliarsuup Qaqqaa shows down throw of a southern hanging wall towards the south-east. This normal fault developed during the Rinkian orogeny, and accounts for
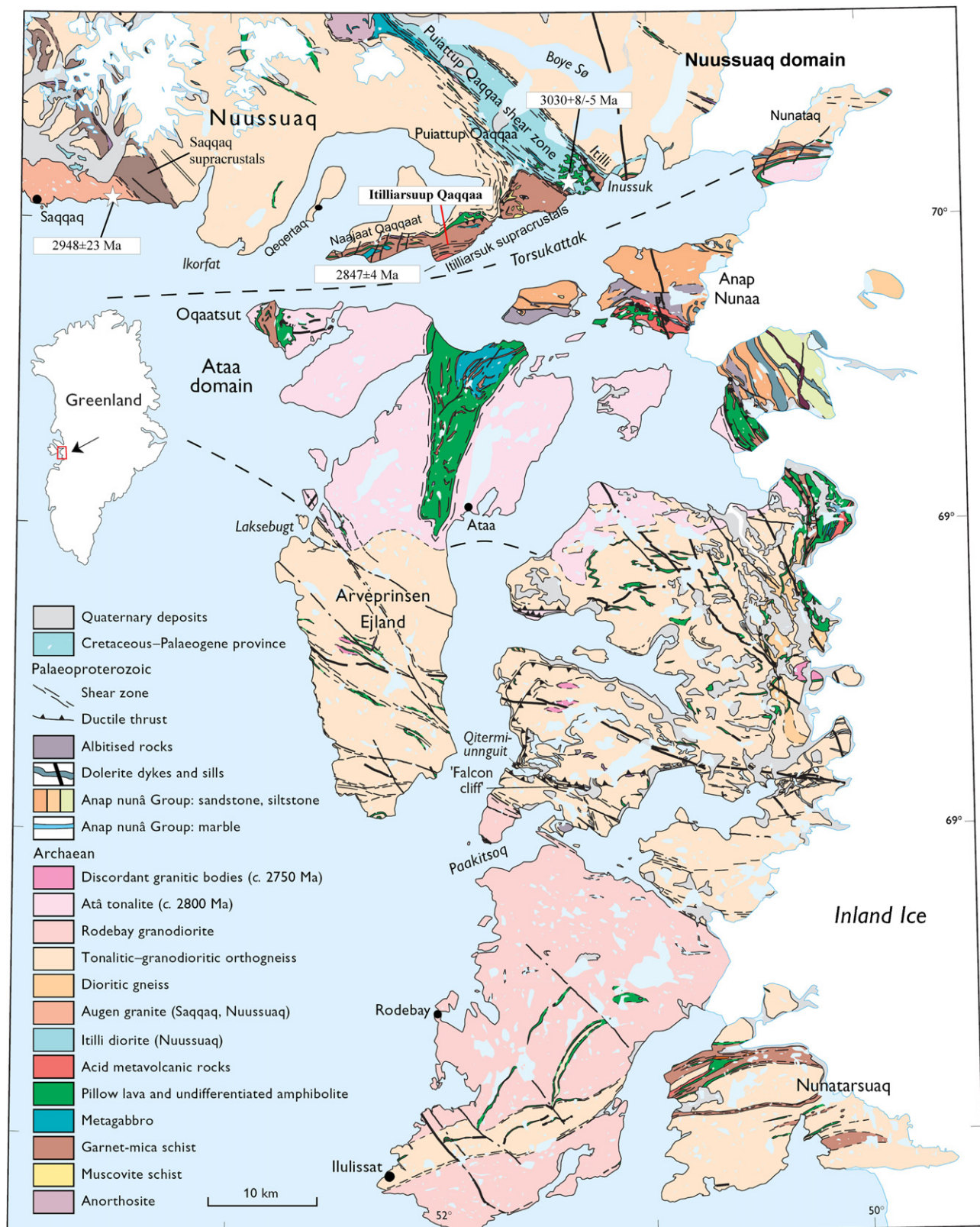
Fig. 1. The main geology in the Disko Bay area. The Itilliarsuk BIF is exposed at the Itilliarsuup Qaqqaa promontory, which is part of the Itilliarsuk supracrustal rocks. The inserted ages are U–Pb zircon ages obtained by Connelly et al. (2006). See text for further details. Dash lines: domain boundaries.
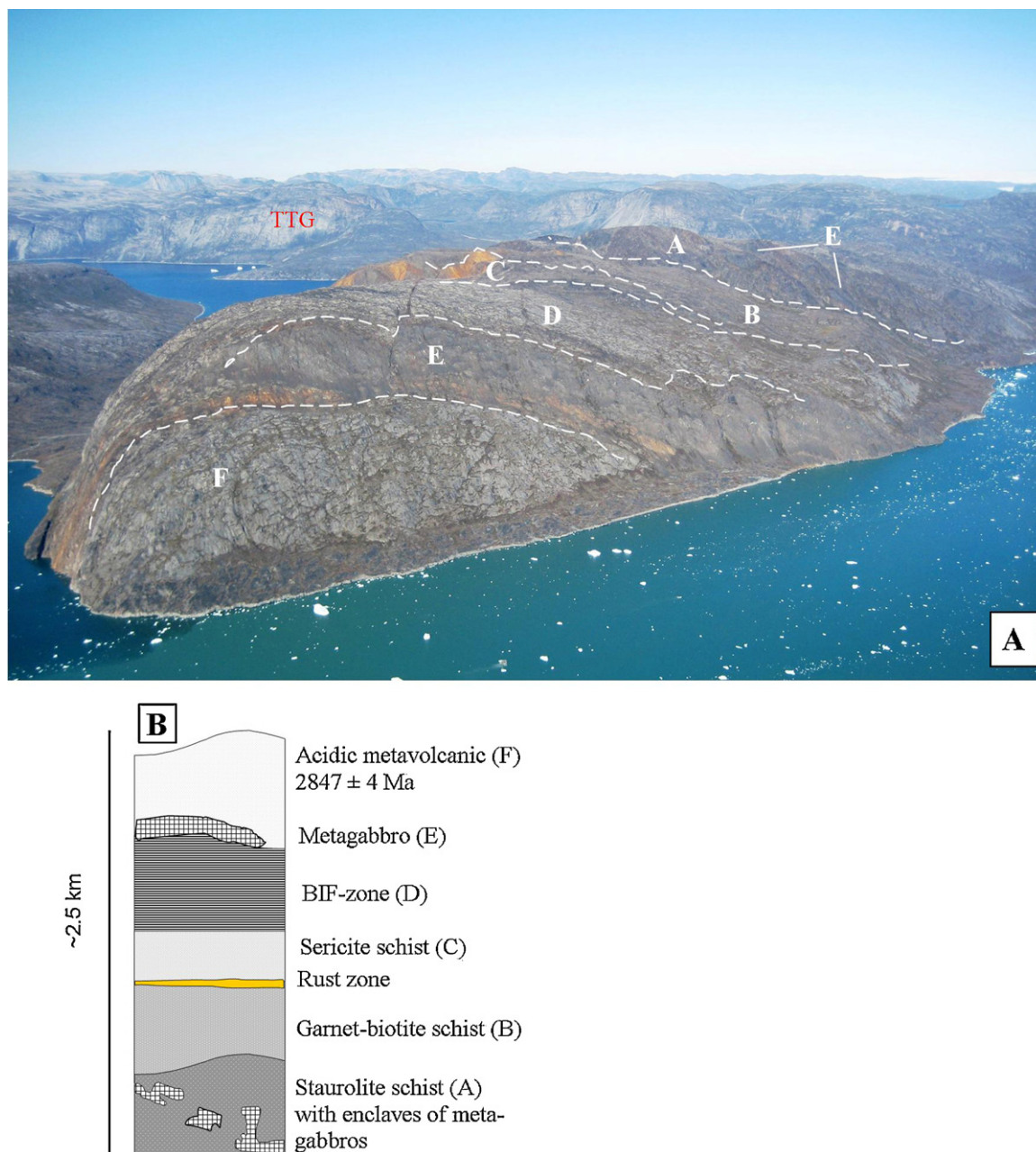
Modified from Garde et al. (2002).

Fig. 2. (A) Field photo of the supracrustal sequence at Itilliarsuup Qaqqaa. Taken towards North. The main lithological units are subscribed with capital letters and linked to the general stratigraphy presented in (B). The Itilliarsuk BIF is exposed within the BIF zone, which constitutes the central part of the promontory. A black >10 m thick part of the BIF can be seen at the summit, approximately 600 m above sea level. Note the grey orthogneiss (TTG) in the horizon. This unit comprises the basement for the Itilliarsuk supracrustals.

the differences in the degree of the tectono-metamorphic regime across the Torsukattak ice-fjord where the footwall Nuussuaq domain experienced a higher degree of Palaeoproterozoic deformation and metamorphism than the hanging wall Ataa domain (Garde and Steenfelt, 1999; Garde et al., 2002; Connelly et al., 2006). During the Palaeoproterozoic Rinkian orogeny, all Archaean rocks in the Nuussuaq domain reached low to intermediate amphibolite-facies metamorphism. In the eastern Nuussuaq, resetting of K–Ar isotopes measured in hornblende yield a range of 1750–1925 Ma, and show that a minimum temperature of ca. 550 °C was reached in this part of the Nuussuaq domain (Rasmussen and Holm, 1999).

Major parts of the Precambrian basement of the Nuussuaq domain consist of Archaean lithologies. The Nuussuaq gneisses predominate where the common type is a light grey homogenous orthogneiss of tonalitic to trondhjemitic composition (Garde and Steenfelt, 1999).

Along the whole south-east coast of Nuussuaq (Fig. 1), the sequences of Archaean supracrustal rocks retain similarities in stratigraphy and structures from Nunataq (towards the East), to the Itilliarsuk supracrustal rocks, and to the Saqqaq supracrustal rocks (towards the West). This led Garde and Steenfelt (1999) to postulate that they originally were one continuous group of supracrustals. The sequences have features similar to Archaean greenstone belts with ultramafic to mafic rocks in the low part, and more siliciclastic metasediment and acidic metavolcanics in the top part (Connelly et al., 2006). The boundary between the supracrustals and the Nuussuaq gneiss is intensely tectonised and sheared and no clear basal unconformity has been found. However,

Table 1
The identified and collected lithologies at Itilliarsuup Qaqqaa.

Lithological units	Sample numbers
The BIF-zone	
Banded iron formation (BIF)	514902, 514926, 514928, 514935
Felsic schist	514910, 514922, 514925, 514927
Quartz–biotite–garnet schist	514908, 514909, 514931
Ferruginous shale	514911, 514932
Amphibole layers within the BIF	514901, 514923
Outside the BIF-zone	
Sericite schist	514920
Garnet–biotite schist	514916
Staurolite schist	514914
Metagabbros	514903, 514904, 514907, 514917
Acidic metavolcanic	514933
Orthogneiss (TTG-basement)	514934

conglomerates with boulders of orthogneiss, located just 500 m south of the supracrustal-gneiss contact, suggest that the Itilliarsuk supracrustal rocks were deposited unconformably on a basement of Nuussuaq gneisses. Furthermore, quartz-rich metasediments close to the basement-cover contact east of Itilliarsuup Qaqqaa indicates provenance from presumably orthogneiss-suite lithologies (Garde and Steenfelt, 1999).

Based on detailed mapping of Itilliarsuup Qaqqaa, Petersen (1997) observed that the Itilliarsuup Qaqqaa consists of felsic schists intermixed with the iron formation, acidic metavolcanics and amphibolites. Similar to the acidic metavolcanic at the top of the sequence, the sericite schist was also interpreted as a fine-grained acidic metavolcanic unit (Petersen, 1997).

Garde and Steenfelt (1999) found that (1) north of the Itilliarsuup Qaqqaa, above the sheared contact to the underlying gneiss, amphibolites with pods of ultrabasic rocks predominate; (2) cross- and graded-bedding found in a metasandstone in the Itilliarsuk supracrustals about 8 km east of Itilliarsuup Qaqqaa suggest that the supracrustals are orientated right way up, and indicate younging upwards in the stratigraphy from the northern gneiss contact and towards SSW (Fig. 2); (3) the central part of Itilliarsuup Qaqqaa is dominated by metasedimentary rocks; and (4) the amphibolites were interpret as metagabbroic sills. Metagabbroic sills are also known from the related supracrustals at Naajaat Qaqqaat, a few km west of Itilliarsuup Qaqqaa (Fig. 1). Rasmussen and Pedersen (1999) characterised these metagabbros as being Mg- and Fe-tholeiites that likely originated in a back-arc setting. Furthermore, they utilised discrimination diagrams for the metasediments at Naajaat Qaqqaat, and suggested a continental island arc as the main tectonic setting. The same authors also discovered small disconnected layers, <1 m thick, of banded iron formation within the sequence.

Important geochronological work in the region was carried out by Connelly et al. (2006). On the south-coast of Nuussuaq, three U–Pb zircon ages were obtained (Fig. 1). The acidic metavolcanic unit at the snout of promontory yielded a U–Pb zircon age of 2847 ± 4 Ma. This age corresponds to the crystallisation time, hence, it represents the minimum age of the Itilliarsuup Qaqqaa succession according to the general stratigraphy in Fig. 2B. Ages were also determined on the basement orthogneiss underlying the Saqqaq supracrustal belt (2947 ± 23 Ma) and the intrusive Itilli diorite ($3030 + 8/-5$ Ma). The latter is a likely minimum age of the orthogneiss at this location (Connelly et al., 2006).

2.1. Field observations

Based upon field observations, only samples from the least altered and deformed outcrops were obtained. A sample table is shown in Table 1 and a geological map with sample locations and an overall scheme with lithological field observations are presented in Fig. 3 and Table 2, respectively. Note the occurrences of garnet in the lower part of the BIF succession and the occasionally appearances of amphibole layers, indicating that the Itilliarsuk BIF experienced medium-grade metamorphism (cf. Klein, 2005).

3. Methodology

A total of 34 samples were studied and collected from 25 sites (see geological map in Fig. 3). Of the 34 samples, 23 samples are included in the present study. The basement gneiss, sample 514934, was collected from the settlement of Qeqertaq located WNW from the Itilliarsuup Qaqqaa (see map, Fig. 1). Selected hand specimens were cut into 1 cm thick slices perpendicular to the foliation. From those slices, a representative area was selected for a final thin section. The thin sections were produced with a target thickness between 27 and 33 µm. All thin sections were made at the laboratory facilities at the Geological Survey of Denmark and Greenland (GEUS).

For geochemical analyses, eight bands were separated from sample 514902 (Fig. 4A) by using two diamond saws at the laboratory of GEUS. From sample 514935 (Fig. 4B), collected by Nunaoil A/S in 1996, 10 bands (five iron-rich and five silica-rich) were separated by using a hand held dremel machine with a small diamond disc (1 cm in diameter) attached. The very fine lamination of samples 514926 and 514928 (Fig. 5C) prohibits any separation of silica- and iron-rich bands. Instead these were analysed as bulk rocks. The BIF and the associated rocks were cut into small chips and subsequently crushed to rock powder using a small agate mortar.

In total 20 BIF samples (including two bulk-BIF) and 13 of the associated rocks (four felsic schists, two quartz–biotite–garnet schists, the garnet–biotite schist, the staurolite schist, the TTG-basement and four metagabbros) were analysed for major elements, trace elements and Nd and Pb isotopes. The acidic metavolcanic and the sericite schist are included in the isotope analyses only. Three BIF samples (Lok83-A, Lok83-B, Lok83-C), collected by Nunaoil A/S in 1996, are included in the Nd isotopes. The major elements were measured on powder tablets by X-ray fluorescence spectrometry (XRF) at the Institute of Geography and Geology, University of Copenhagen. Major elements are presented on a LOI-free basis, thus, there may be small discrepancies between the "real" concentration values and the computed ones. Fe^{2+}/Fe_{total} ratios were measured solely on the BIF samples. Reproducibility on the concentration is better than 10%.

Trace element concentrations were measured by Inductively Coupled Plasma Mass Spectrometry (ICP-MS). 50 mg rock powders from each sample were digested using standard dissolution procedure. To avoid precipitation of Fe^{3+} on the cones and, hence disturb the magnetic field, all BIF samples were further diluted with 5 ml 0.7% HNO_3 before loading. The solutions were analysed with a Perkin Elmer ELAN 6100 DRC spectrometer at GEUS. All results are compared to the repetitive analyses of the BVHO2-standard. The accuracy on the measured concentrations is within 5–10%. Sample 514928 has been rejected due to difficulties in the dilution procedure.

Concentrations of REYs in the BIF samples were normalised to Post-Archaean Average Shale (PAAS) after Taylor and McLennan (1985). REE for the non-BIF lithologies were Cl chondrite-normalised according to Anders and Grevesse (1989). Potential anomalies of La and Ce were obtained by the procedure proposed by Bolhar et al. (2004): $La/La^* = La/[3Pr - 2Nd]$ and $Ce/Ce^* = Ce/[2Pr - 1Nd]$. The cerium-anomaly was calculated without the use of lanthanum due to generally elevated values of La in ocean waters relative to neighbouring LREE (Bolhar et al., 2004). In agreement with Alexander et al. (2008), the Eu-anomaly was calculated as $Eu/Eu^* = Eu/[0.67Sm + 0.33Tb]$. Accurate determination

Table 2
Field observations of the BIF and the associated lithologies at Itilliarsuup Qaqqaa.

The BIF zone	Outside the BIF zone	Description
Banded iron formation (BIF)		The BIF has an exposed strike (E–W) length of c. 3–4 km and a width of c. 700–1000 m. Although weathered surfaces do occur locally, the whole BIF formation generally appears very fresh and unweathered. It consists of very fine-grained bulk bands ranging from less than 1 cm to 15 m in thickness. The Fe-rich bands are black, highly magnetic, and are generally finely laminated with 1–2 mm bands of microcrystalline quartz (Fig. 5A–C). The peak of the promontory comprises the central part of the BIF zone, where BIF is most abundant and the magnetite bands are thickest. Here the BIF form ridges which are highly resistant to weathering (Fig. 2A) and where the individual magnetite-bearing bands are intercalated with the felsic schist unit (Fig. 5A and B). The contact between the felsic schist and the BIF is sharp, straight, and well-defined with no sign of any grading, erosion or intermixing (Fig. 5A and D). Towards north-east the magnetite bands diminish and the quartz bands increase up to 1.5 cm in thickness (Fig. 5D). Along the eastern shoreline the BIF is only a few cm thick, and intercalated with beds of ferruginous shale, quartz–biotite–garnet schist and minor felsic schist. In the north-eastern part of the BIF zone, concentrations of up to 1 cm anhedral garnets occurs at the interface between the BIF and the quartz–biotite–garnet schist. Occasionally, these garnets are also formed within the BIF (Fig. 5E), Despite the general very fine microbanding in the Itilliarsuk BIF, two samples (samples 514902 and 514935) with individual bands suitable for separation have been collected. The two samples are presented in Fig. 4 where the individually bands are marked with letters
Felsic schist		This lithology consists predominantly of quartz, muscovite and biotite. The dominating grain size ranges from fine-grained (<1 mm) to medium-grained (2 mm). The texture is very homogenous and massive with no preferred lamination or grading. Within the dense BIF zone in the central part of the promontory, the magnitude of individual layers vary from 5 cm and up to 10 m stacked between the BIF (Fig. 5A and B)
Quartz–biotite–garnet schist		Consist predominantly of 3–5 mm subhedral porphyroblasts of garnets set in a fine-grained (<1 mm) matrix of quartz and biotite (Fig. 6E). It is faintly laminated with fine (~1 mm) biotite and quartz-rich layers. On the boundary to the upper felsic schist unit, the grain size and the modal content of quartz increases while the biotite content decreases. The unit is most pronounced in the northern and eastern part of the BIF zone where BIF is less representative. The thickness of the unit varies from tens of cm to tens of metre. Locally the unit is silicified
Ferruginous shale and schist		Variegated Fe-rich sediments are exposed along the eastern coast. Dark grey ~3–5 cm thick beds of fine-grained iron-rich shale predominate. A black 2 m thick sequence of coarse-grained biotite– and garnet-rich schist occurs. The up to 1 cm euhedral garnets constitute as much as 30% of the rock by volume
Amphibole layer		Although volumetrically less significant, 1–2 cm thin boudinage layers of greenish amphiboles, occasionally containing garnets, occur (Fig. 6A). These layers are found concordant interbedded within the BIF
	Sericite schist	The term sericite schist implies a rock that is rich in fine-grained white mica. Volumetrically, this unit may not be as significant as previously mapped. It represents a fine-grained micaceous schist, which is faintly laminated (<1 mm) and consist predominantly of quartz, sericite and biotite. Whether the fine-grained mica is an alteration product of feldspars is unknown due to the fine-grained texture. Disseminated, both primarily and oxidised, sulphides are found adjacent to the sulfidic rust zone (Fig. 2)
	Garnet–biotite schist	Contains up to 1 cm dark red, euhedral garnets hosted within a fine- to medium-grained biotite– and quartz-rich matrix. The garnet porphyroblasts constitute ~10% of the rock volume. Due to the relatively high biotite and garnet content the lithology often has a rusty appearance
	Staurolite schist	Dark and well-developed staurolite crystals occur in a medium-grained matrix of mainly muscovite. The euhedral staurolite crystals vary in size from 6 to 7 cm large porphyroblasts to a few mm (Fig. 6F). They constitute about 10% of the rock volume, but up to 25% have been found locally. The staurolite shows perfectly ~60° twin growth. The transition from the garnet–biotite schist to the staurolite schist further north is seen in a gradual change with garnet disappearing and staurolite increasing in abundances, whilst the biotite content decreases and the grain size is slightly increased
	Metagabbro	Towards the south of the field area, a dark green, medium (few mm) to coarse-grained (5–7 mm) metagabbro terminates the BIF zone. This unit shows strong schistosity with a linear amphibole–fabric orientated in the direction of stretching (Fig. 6D). Irregular, 1–2 mm (occasionally 5–10 mm), thin silica veins are found sporadically. In the Western end of the unit the metagabbro is carbonate altered expressed as a brownish, rusty appearance with ropy-like structures. Faintly mm-layers of secondary biotite are found at few places. At one location, the bulk of the metagabbro (red arrow in Fig. 6B) has intruded the BIF (white arrows in Fig. 6B). Close to the western end of the unit a well exposed surface with garbenschiefer texture is found. Enclaves of metagabbros occur within the staurolite schist in the northern part of the area. These are very coarse-grained (~10 mm), dark to dark-green rock with only weak schistosity (Fig. 6C). Euhedral amphiboles predominate, whereas medium-grained (1–3 mm) plagioclase only occurs sporadically. Few quartz-schlieren are present throughout
	Acidic metavolcanic	Located at the outermost snout of Itilliarsuup Qaqqaa. The rock is pale grey, fine-grained and homogenous. Some flow banding features are recognised. The outcrop shows a preferred steep lineation in the SE-direction. This rock unit yields a 2847±4 Ma U–Pb zircon-age (Connelly et al., 2006) and comprises the upper and youngest section of the Itilliarsuup Qaqqaa supracrustal succession (Fig. 2)
	Orthogneiss (TTG-basement)	To better constrain the depositional environment and source characteristics for the BIF and the related rocks, inclusion of the basement orthogneiss is essential. The gneiss is pale grey, rather homogenous, non-migmatitic and consists mainly of medium-grained (2–5 mm) quartz, plagioclase and biotite. A minimum age between 2947±23 and 3030+8/−5 Ma has been dated by Connelly et al. (2006)

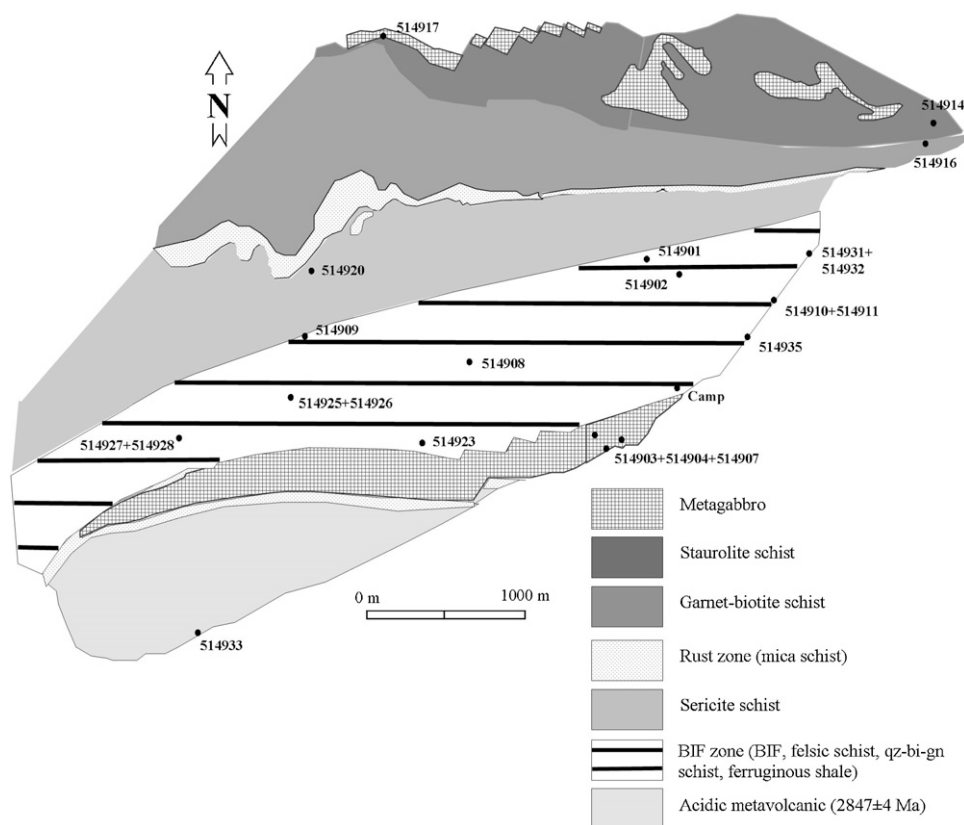**Geological map of Itilliarsuup Qaqqaa 1:10.000**

Fig. 3. The geological map of Itilliarsuup Qaqqaa with sample locations. Map modified and redrawn from Petersen (1997).

of Gadolinium (Gd) was difficult due to interference with barium (Ba), consequently, the normalised Gd-values in the REY-diagrams were calculated as Gd* = [0.33Sm + 0.67Tb]. In the REY-diagrams, yttrium is inserted between Dy and Ho, according to decreasing ionic radii of the three elements.

Nd and Pb isotope ratios were obtained with a VG Sector 54 IT mass spectrometer at the Institute of Geography and Geology, University of Copenhagen. Samples were dissolved following the same procedure as for the trace element solution. Separation of Pb was done over anion exchange columns containing Bio-Rad

AG 1*8 100–200 meshes. During Pb isotope analyses the mass spectrometer was operated in static mode and repeat analyses of the NBS 981 standard yielded a fractionation factor of $0.105 \pm 0.008\%$/amu (2σ, $n = 5$). The Pb blanks were <48 pg, implying that the blanks had an insignificant influence on the measured Pb isotope ratios. For Sm and Nd analyses a 150 mg ^{147}Sm/^{150}Nd spike was added to the rock powder before dissolution. Separation of REE was done over cation exchange columns containing AG50W-X8, 100–200 mesh resins. Sm and Nd were further separated from the collected REE using glass columns containing LN resin SPS. The
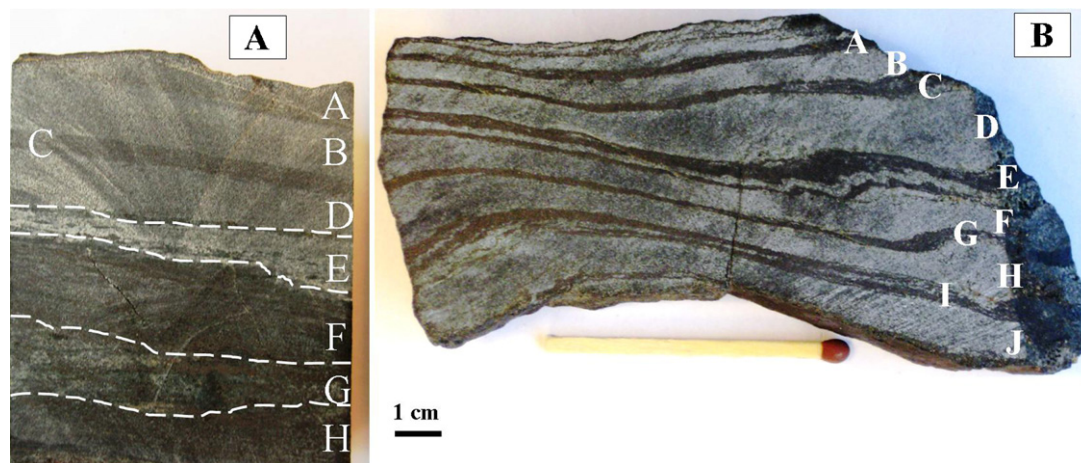
Fig. 4. Individually micro- and mesobands from the Itilliarsuk BIF analysed in this study. (A) Sample 514902 and (B) sample 514935. The latter sample comprises more well-defined alternating Fe-rich and silica-rich bands.
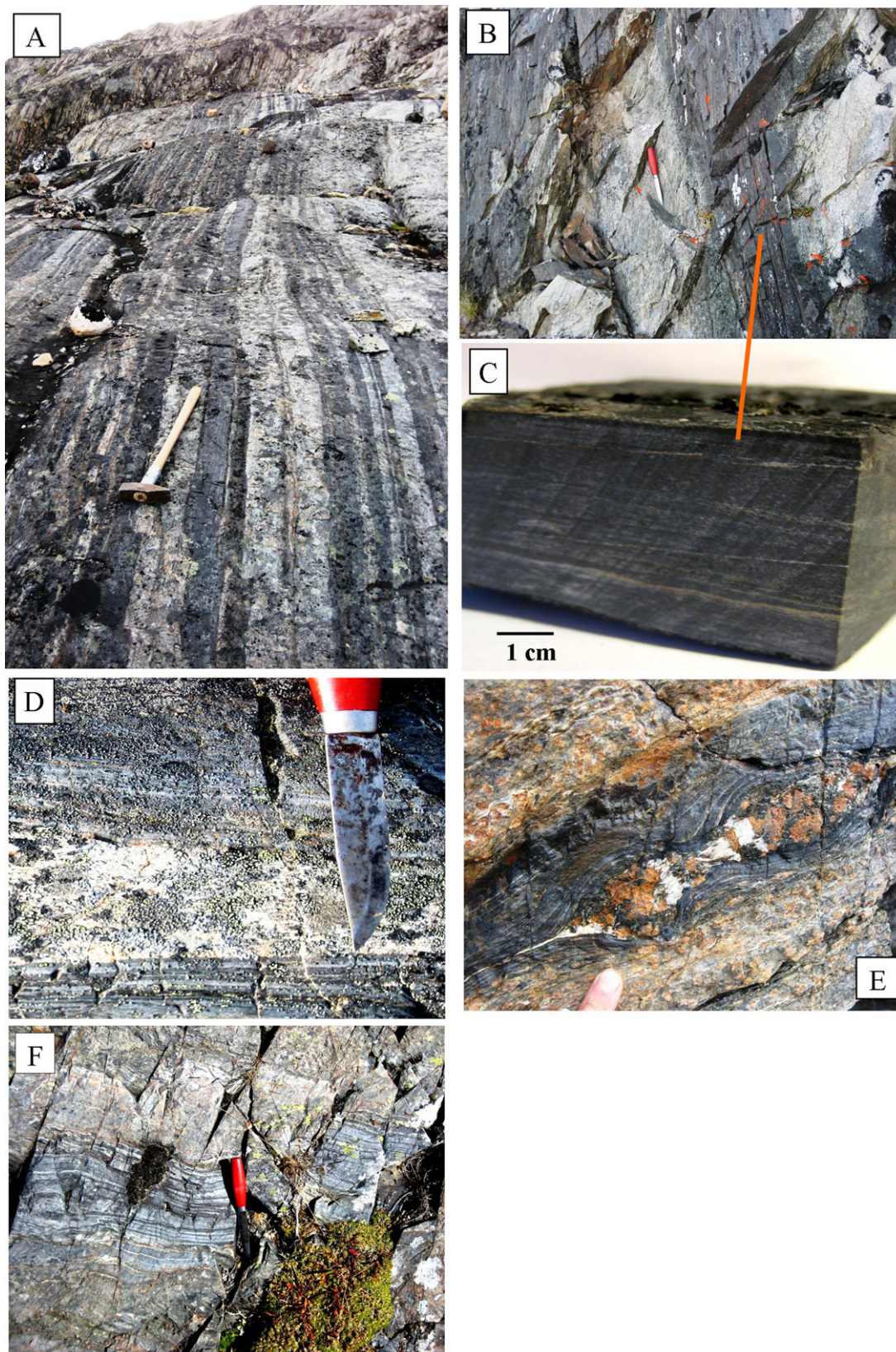
Fig. 5. Field photos of the Itilliarsuk BIF. (A) Black bands of magnetite-rich iron formation intercalated with the felsic schist unit. Note the very straight and linear contact between the two lithologies. Hammer = 65 cm. (B) From the top part of the Itilliarsuup Qaqqaa revealing very dense magnetite bands interbedded with the felsic schist unit (knife). Samples 514927 and 514928 are collected from this location. (C) Close up of the BIF from the sample site in (B). Note the very fine laminae of chert. (D) Close up of the BIF with very smooth and regular contact to the felsic schist. (E) Garnet-rich boudinage within a BIF horizon. Taken from the north-eastern BIF zone where the BIF is interbedded with the quartz–biotite–garnet schist. (F) Field photo taken further east in the BIF zone where the silica-rich bands increase in thickness and the Fe-rich bands become more well-defined. (Refer to Table 2 for more detailed field descriptions).
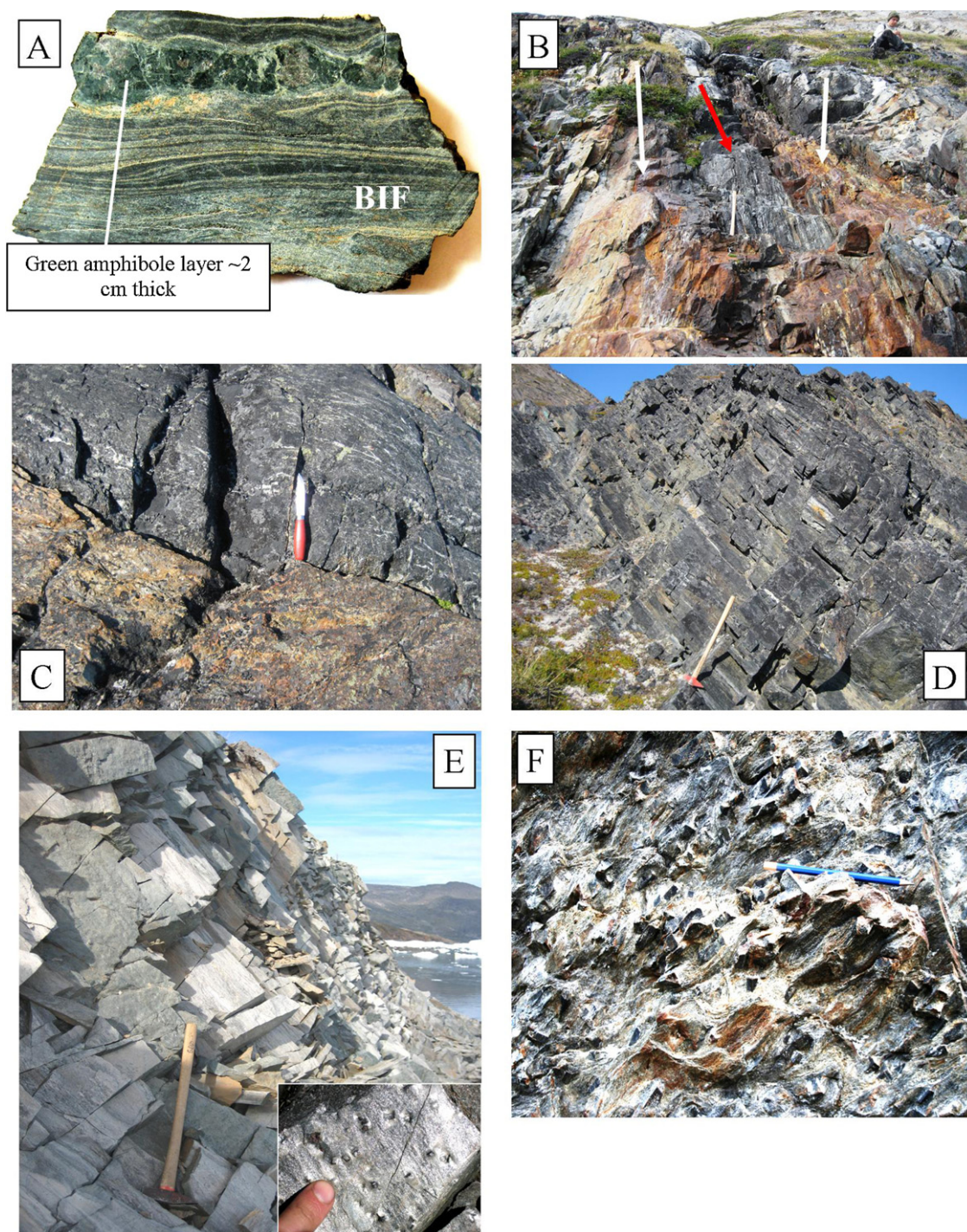
Fig. 6. Field photos of selected associated lithologies at Itilliarsuup Qaqqaa. (A) Fresh surface showing boudinage structure of a green amphibole layer with few garnets developed. Found concordant within the BIF. (B) A body of metagabbro (red arrow) identified within the magnetite-rich BIF (white arrows). Taken close to the contact between the southern metagabbro and the BIF zone. (C) Enclave of the northernmost coarse-grained metagabbro (sample 514917) within the staurolite schist. Note the content of quartz-schlieren. (D) The southern metagabbro showing high schistosity and steeply southern dip. Taken towards north-east. (E) The fine-grained quartz–biotie–garnet schist. Insert close-up photo shows few mm garnets. Taken from the east coast of the promontory looking towards north-east. Note again the steep dip below the Torsukattak ice-fjord to the right in the picture. (F) Very coarse-grained porphyroblasts of staurolite from the staurolite schist, which indicate medium-grade amphibolite metamorphism. (Refer to Table 2 for more detailed field descriptions). (For interpretation of the references to color in this figure legend, the reader is referred to the web version of the article.)

Nd isotope ratios were analysed dynamically whereas Sm was run static. The Nd isotope ratios were corrected for mass fractionation to $^{146}Nd/^{144}Nd = 0.7219$. Precision on $^{147}Sm/^{144}Nd$ is better than 2% (2σ). During the time of measurement the internal mean value of $^{143}Nd/^{144}Nd$ to the JNDI-standard was 0.512099 (2σ, 21 ppm).

The age used for calculating the initial $^{143}Nd/^{144}Nd$-values was the U–Pb zircon age of 2847 ± 4 Ma obtained by Connelly et al. (2006) for the acidic metavolcanic at the top of the sequence. The initial epsilon notation $\varepsilon_{Nd}(2847 \text{ Ma})$ will be subscribed $\varepsilon_{Nd}(i)$. T_{DM} ages were calculated according to DePaolo (1981).

Fig. 7. Micro-photographs of the BIF and the related felsic schist. (A), (B) and (C) taken with crossed polars of the BIF while micro-photographs (D), (E) and (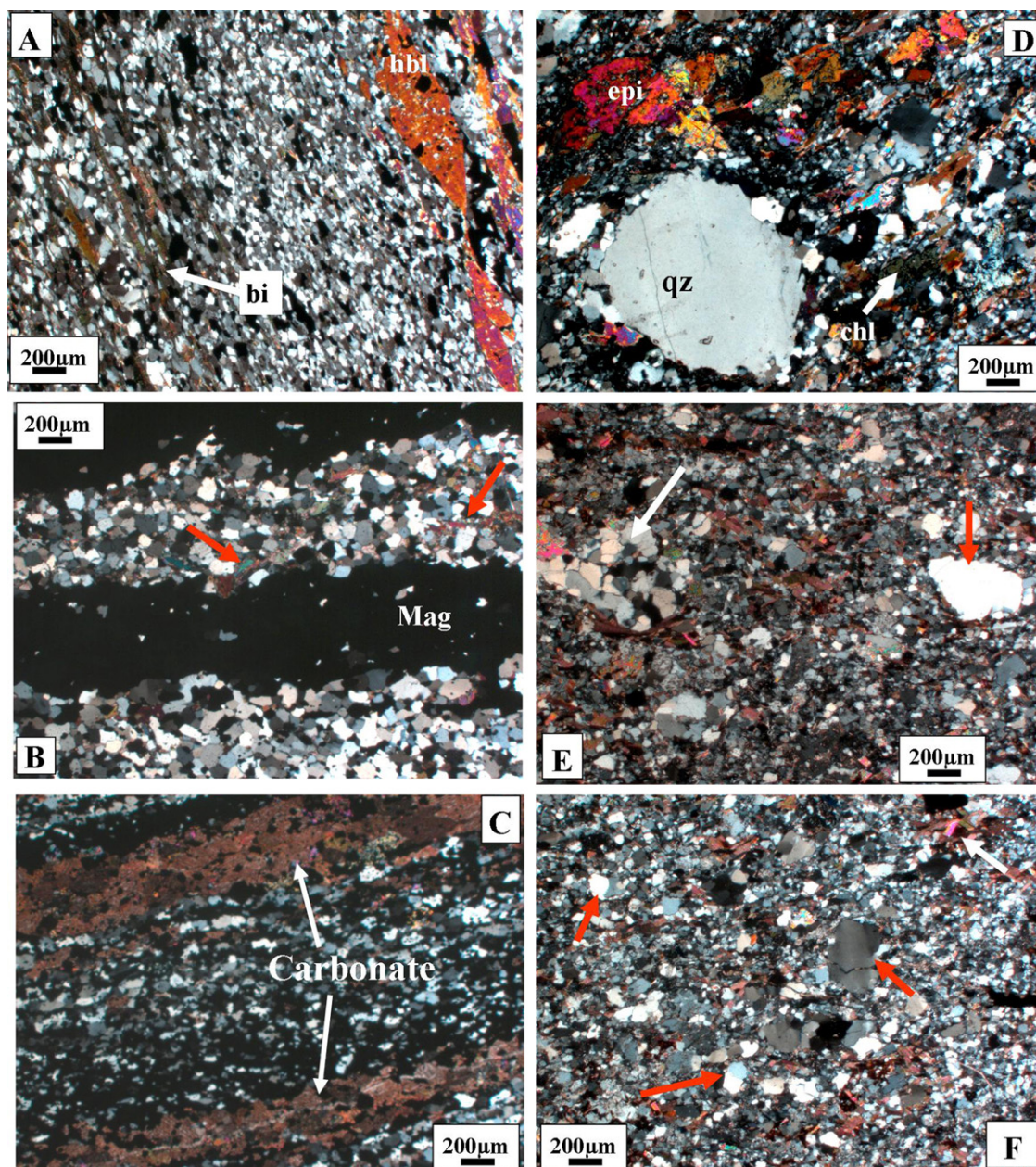F) are taken with crossed polars of the felsic schists. (A) Sample 514902. Shows relatively high biotite content and large sub- to euhedral hornblende. (B) Sample 514935. Shows distinct silica- and Fe (magnetite)-rich bands and small amphiboles primarily developed in the silica-rich bands (red arrows). (C) Sample 514928. Beside the magnetite and quartz, this sample also contains white, and in this case brownish, concordant carbonate layers. (D) Randomly distributed quartz, epidote, biotite and minor chlorite. Note the large and rounded quartz clast. (E) Shows a large polycrystalline quartz grain (white arrow) and a large monocrystalline quartz grain (red arrow) set in a fine-grained immature quartz and biotite matrix. (F) Chaotically distributed angular quartz grains (red arrows). White arrow displays a zircon fragment. (For interpretation of the references to color in this figure legend, the reader is referred to the web version of the article.)

4. Petrography

Photomicrographs of the overall mineralogical characteristics are shown in Figs. 7 and 8, and the mineral assemblages are summarized in Table 3.

4.1. Banded iron formation

The mineralogy of the Itilliarsuk BIF varies both in contents and proportions. The modal mineral abundances in sample 514902 (Fig. 7A) are quartz (40–50%), magnetite (25–30%), amphibole (10–15%), biotite (10–15%), chlorite + epidote (1–5%) and accessory plagioclase (<2.5%). The quartz grains are irregularly shaped and

deformed with undulatory extinction. Quartz and magnetite are often intermixed showing only weak banding. Medium-grained (1–2 mm) subhedral hornblende is concentrated in 1–2 mm thin laminae. Epidote and minor chlorite occur where the magnetite dominates, while bladed biotite occurs where the quartz dominates. Up to 4–5 mm laminae of biotite are found locally in the specimen. The amphiboles show strong pleochroism (pale green to dark green to deep bluish green) indicating high iron content. Ferro-hornblende or ferro-actinolite is the likely amphibole phase. In the few well-developed crystals, extinction angle of ~25–35° occurs parallel to (0 1 0) which, together with the general medium-grade amphibolite metamorphism in the area, support the former phase. In contrast, sample 514935 (Fig. 7B), contains a more
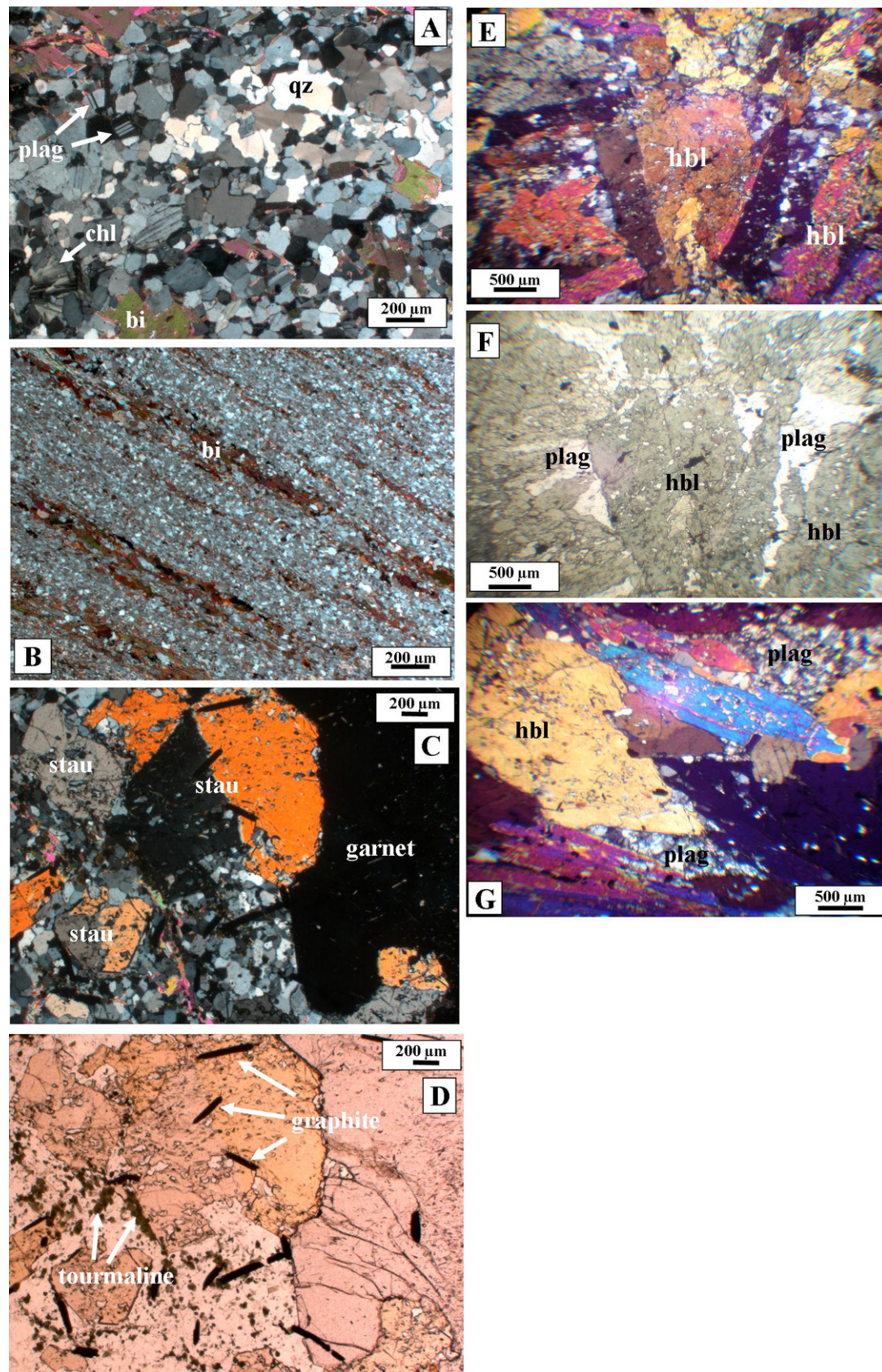
Fig. 8. Micro-photographs of the associated lithologies at Itilliarsuup Qaqqaa. (A) The quartz–biotite–garnet schist taken with crossed polars. Shows fresh and unaltered plagioclase, pseudomorphic chlorite and tabular biotite. (B) Very fine-grained sericite schist with biotite laminae and angular quartz grains set in a gritty sericite- and epidote-matrix. Taken with crossed polars. (C) Micro-photograph showing the mineralogy from the transition between the garnet–biotite schist and the staurolite schist. These two units contain high amount of aluminium- and iron-rich minerals. Note the twinning in the staurolite. Taken with crossed polars. (D) Same as in C, but taken in plane-polarised light. Note the elongated graphite. (E and F) Metagabbro (sample 514904) showing coarse-grained hornblende with small pockets of plagioclase. Taken in plane-polarised light. (G) Metagabbro (sample 514917) showing the same texture as sample 514904, but with even larger hornblende crystals.

Table 3
The mineralogical compositions identified in the lithologies at Itilliarsuup Qaqqaa.

Lithological units	Mineral assemblages
Banded iron formation (BIF)	Quartz + magnetite + ferro-hornblende ± ferro-actinolite ± biotite ± garnet ± epidote ± chlorite ± calcite ± plagioclase
Felsic schist	Quartz + biotite + epidote + plagioclase + muscovite + sericite + sphene + zircon ± garnet
Quartz–biotite–garnet schist	Quartz + biotite + garnet + plagioclase + chlorite + opaque accessories
Sericite schist	Quartz + sericite + biotite + calcite + epidote + muscovite + amphibole + garnet + chlorite
Staurolite schist	Quartz + muscovite + staurolite + plagioclase + chlorite + graphite + sphene + tourmaline + apatite + zircon ± calcite
Garnet–biotite schist	Quartz + biotite + garnet + plagioclase + tourmaline + staurolite + graphite + muscovite + zircon
Metagabbros	Hornblende + plagioclase + quartz + sphene + opaque Fe–Ti oxide + chlorite ± biotite

simple mineralogy having only quartz (55–65%), magnetite (30–35%) and amphiboles (5–10%) as dominant phases. The microcrystalline quartz creates a tight mosaic with angular to sub-angular grains whereas the fine-grained (0.1–0.2 mm) amphiboles generally have an anhedral habitus. The magnetite microbands are compact with sharply defined boundaries to the silica-rich mesobands. The two BIF samples collected for bulk analyses, samples 514926 and 514928 (Fig. 7C), contain quartz (40–50%), magnetite (35–45%), amphibole (5–10%) and minor calcite + chlorite + biotite (1–5%). These BIF types have only weakly defined lamination with few distinct (1–2 mm) silica-rich and magnetite-rich microbands. A noteworthy observation is that magnetite and quartz are occasionally inter-layered with few white and pale brown 1–2 mm thin carbonate layers. These horizontal layers react heavily to cold diluted HCL, suggesting a calcitic component. The amphibole rich BIF mesobands, represented by samples 514901 and 514923, consist of amphibole (80–90%), garnet (10–15%), accessory calcite + epidote (1–5%). The amphiboles are coarse-grained (5–10 mm) and show pronounced pleochroism, from light green to deep greenish blue, and contain inclusions of allanite.

4.2. Felsic schist

These rocks contain quartz (55–65%), biotite (10–15%), feldspar (5–10%), muscovite (5–10%), sericite (1–5%), chlorite, epidote and opaque accessories (1–5%) (Fig. 7D–F). Approximately 40 vol% of the rock consists of medium-grained (0.1–2 mm) angular fragments of quartz, biotite, epidote and feldspar randomly dispersed in a 60 vol% fine-grained (<0.1 mm) quartz and mica-rich matrix. The framework quartz is predominantly monocrystalline (grains composed of a single crystal, red arrow in Fig. 7E), but minor polycrystalline grains (composed of two or more crystals) occur (white arrow in Fig. 7E). The quartz grains are generally angular to sub-angular (red arrows in Fig. 7F), but a minor portion of the medium-grained monocrystalline grains is spherical and well-rounded (large quartz clast in Fig. 7D). Fine- to medium-grained sub-angular feldspar with minor sericite alteration is found throughout. Epidote and minor chlorite are most likely pseudo-morphs after tabular mafic minerals (Fig. 7D). A fragmented zircon is seen in Fig. 7F (white arrow).

4.3. Quartz–biotite–garnet schist

These schists contain quartz (40–50%), biotite (20–30%), muscovite (5–10%), plagioclase (5–10%), garnet (5–10%), chlorite (1–5%), opaque accessories (<2.5%) (Fig. 8A). The quartz grains are inequant and monocrystalline showing both strained and unstrained properties. Biotite often forms continuously elongated flakes with a preferred crystallographic orientation. Associated with the biotite flakes, thin needles of chlorite are developed. Biotite flakes are wrapped around inclusion-rich garnet porphyroblasts. Tabular biotite and chlorite are found locally and the feldspar (mainly plagioclase) is fresh and unaltered (Fig. 8A).

4.4. Sericite schist

It contains quartz (30–40%), biotite (10–20%), sericite (10–20%), muscovite (5–10%), epidote (5–10%), amphibole (1–5%), garnet (1–5%), calcite (<2.5%) and chlorite (<2.5%) (Fig. 8B). The rock is very fine-grained with a few porphyroblasts of altered amphiboles and garnets. Laminae of bladed biotite occur in a matrix of sub-angular quartz, sericite and epidote. The degree of alteration is relatively high as expressed by layers of pseudomorphic chlorite and secondary inter-granular calcite grains. With the fine-grained texture and millimetre-scale lamination, this unit has, as previously proposed by Petersen (1997), features that suggest an acidic volcanic rock precursor.

4.5. Garnet–biotite schist

This schist comprises quartz (25–35%), biotite (20–30%), plagioclase (10–15%), garnet (10–15%), tourmaline (1–5%), staurolite (1–5%), muscovite (1–5%) and graphite (<2.5%) (Fig. 8C and D). The quartz is monocrystalline, with minor undulatory extinction and often shows perfect triple junctions between the grains. Fresh and unaltered sub-angular plagioclase occurs throughout. In the groundmass, between garnet porphyroblasts, very fine-grained tourmaline occurs. These vary in size from 5 to 100 μm, showing no preferred orientation and are often concentrated as euhedral prismatic crystals close to garnets and staurolites. The tourmaline grains appear unzoned which point towards a metamorphic origin. Subhedral zircons are found intermixed with crystals of tourmalines. The poikiloblastic staurolites contain quartz inclusions and display well-developed 60° twins. Elongated blades of opaque graphite are chaotically distributed throughout. A few apatite grains are found within flakes of muscovite.

4.6. Staurolite schist

It contains quartz (20–30%), muscovite (20–30%), plagioclase (10–20%), staurolite (10–15%), chlorite (5–10%), graphite (<2.5%), tourmaline, zircon, sphene and apatite (<2.5%). The staurolite porphyroblasts are wrapped in thick flakes of muscovite. Some of the staurolite crystals have partly reacted and formed garnets. Elongated chlorite is found throughout, presumably as pseudomorph after biotite. Graphite is dispersed as in the garnet–biotite schist.

4.7. Metagabbro

Samples 514904 and 514917 contain hornblende (75–85%), plagioclase (10–15%), quartz (1–5%), opaque accessories (<2.5%), chlorite and sphene (<2.5%) (Fig. 8E–G). The hornblendes appear relatively fresh (except along few cracks where retrograde chlorite occurs), and are coarse- (5–10 mm) to very coarse-grained (>10 mm). Fine-grained (0.1–0.2 mm) plagioclase occurs as inter-granular pockets between the euhedral hornblendes (Fig. 8F and G). Sphene and opaque phases, presumably Fe–Ti oxides, occur mainly within the hornblende. Samples 514903 and 514907 are

more altered with randomly distributed calcite and silica veins and the hornblende being partly dissolved and substituted by chlorite.

5. Geochemical results

5.1. Major and trace elements

Concentrations of major elements and selected trace elements in the Itilliarsuk BIF are displayed in Tables 4A and 4B, respectively. Elemental correlation diagrams are shown in Fig. 9A–D, and PAAS-normalised REY-diagrams are shown in Fig. 10A and B, respectively. Major elements and selected trace elements from the associated rocks are presented in Table 5, and chondrite-normalised REE patterns are displayed in Fig. 11. The different schist types were all screened for potential post-depositional silicification and K-metasomatism. The degree of silica and potassium enrichment is minor, which is expressed by the overall low ratios of K_2O/Na_2O (<1) and SiO_2/Al_2O_3. These ratios are consisting with Archaean metasediments in general (Veizer and Mackenzie, 2003; Bolhar et al., 2005).

5.1.1. Banded iron formation

Of particularly interest is the difference between samples 514902 and 514935. Seven mesobands from sample 514902 are enriched in Al_2O_3, TiO_2, Zr, Nb, Sc, Cr, V and Ni. Only layer 514902H exhibits significantly lower concentrations in these elements. Sample 514935 represents the chemically purest BIF sample with low values of all the above elements, and comprises distinct alternating Si-rich (average 64.5 wt.% SiO_2, with 30.4 wt.% Fe_2O_3) and Fe-rich (average 68.0 wt.% Fe_2O_3, with 29.6 wt.% SiO_2) bands. The aluminium content is lowest in the Fe-rich layers and highest in the Si-rich layers. For all BIF samples, except one, the sulphur content is below detection limit, reflecting a negligible amount of iron sulphide minerals. The $Fe^{2+}/\Sigma Fe$ ratios ($=Fe^{2+}/(Fe^{2+}+Fe^{3+})$) for pure magnetite is 1/3 but the ratios for the Itilliarsuk BIF all lie above this value indicating a second minor phase for the iron. The metamorphic Fe-rich amphiboles could explain the elevated $Fe^{2+}/(Fe^{2+}+Fe^{3+})$ ratios.

In general, strong positive correlation is found between the above immobile elements, which could point to the fact that these

elements were hosted and deposited in the clay-rich fraction and not released to solution. Shown in Fig. 9A–C are Al_2O_3 vs. TiO_2 ($R = 0.976$), Ti vs. Cr ($R = 0.965$) and Zr vs. Cr ($R = 0.954$) respectively. Interestingly, the REYs are decoupled from these elements. This is represented by Fig. 9D where Al_2O_3 vs. ΣREY yielded an R-value of 0.08.

PAAS-normalised REY distribution for sample 514902 is displayed in Fig. 10A, and for sample 514935 in Fig. 10B. On each graph the bulk-BIF (sample 514926) is shown with blue signature. The abundances of REY are comparable with other banded iron formations reported around the world (e.g., the Neoarchaean BIFs from the Black Hills (Frei et al., 2008) and the 2.9 Ga old Pongola BIF (Alexander et al., 2008)). Meso- and microbands from sample 514935 all display LREE depletion relative to HREE ($[Pr/Yb]_{PAAS} = 0.47–0.85$), whereas six of the bands are enriched in MREE ($[Sm/Yb]_{PAAS} = 1.08–1.30$). In contrast, enriched LREE patterns are found in three mesobands from sample 514902 ($[Pr/Yb]_{PAAS} = 1.19–1.43$). The bulk rock (sample 514926) are characterised by flat LREE to HREE patterns ($[Pr/Yb]_{PAAS} \sim 1$) but an enrichment in MREE ($[Sm/Yb]_{PAAS} = 1.35$). All of the analysed BIFs are characterised by positive Eu-anomalies ($[Eu/Eu^*]_{PAAS} = 1.30–1.94$, average 1.63 ± 0.16) and predominantly positive La-anomalies ($[La/La^*]_{PAAS} = 0.94–1.82$, average 1.33 ± 0.23). The Ce-anomalies are mainly positive but highly scattered ($[Ce/Ce^*]_{PAAS} = 0.89–4.93$, average 1.6 ± 0.88). Near chondritic values (~ 26) of Y/Ho are found throughout the majority of the Itilliarsuk BIF samples. In sample 514902 band H records the highest value (31.4), whereas three of the highest Y/Ho values in sample 514935 occurs in the Fe-rich bands (29.9, 30 and 34.1).

5.1.2. Felsic schist

This poorly sorted unit, which is intercalated with the main part of the BIF, comprises average SiO_2/Al_2O_3 ratios of 4.4, Al_2O_3/TiO_2 of ~ 40, $Na_2O/K_2O > 1$ and Rb/Sr ~ 0.11. The concentration of transition elements (Cr, Ni and V) is relatively low. The REE patterns (Fig. 11) have average $[La/Yb]_{CHON}$ ratios of ~ 16 and only weak positive Eu-anomalies ($[Eu/Eu^*]_{CHON} \sim 1.16$).

5.1.3. Quartz–biotite–garnet schist

In comparison with the felsic schist this rock exhibits lower SiO_2 content, higher Fe_2O_3 content (corresponding with

Table 4A

Major elements of the Itilliarsuk BIF. Samples are presented with the last three digits only.

XRF (wt.%)	SiO_2	Fe_2O_3t	Al_2O_3	TiO_2	MnO	MgO	CaO	Na_2O	K_2O	P_2O_5	S	$Fe^{2+}/\Sigma Fe$
Sample												
902A/Si + Al	50.0	35.6	8.40	0.36	0.05	1.23	1.56	1.85	0.82	0.14	nd	0.44
902B/Si + Al	53.8	32.2	8.35	0.28	0.05	1.46	1.45	1.72	0.57	0.16	nd	0.46
902C/im	50.4	42.4	3.50	0.22	0.08	1.11	1.44	0.59	0.11	0.15	nd	0.46
902D/Si + Al	51.8	27.5	12.40	0.44	0.04	1.48	2.48	2.69	1.04	0.18	nd	0.47
902E/Si + Al	54.1	24.3	12.91	0.43	0.06	1.38	3.87	2.46	0.36	0.13	nd	0.46
902F/im	44.3	46.6	4.21	0.21	0.07	1.33	2.36	0.31	0.31	0.21	nd	0.48
902G/im + Al	38.9	43.2	9.51	0.39	0.07	0.70	5.85	0.49	0.63	0.24	nd	0.44
902H/im	48.7	48.2	0.99	0.12	0.05	0.78	0.97	0.07	0.04	0.14	nd	0.44
926/bulk	44.0	50.1	3.22	0.13	0.03	0.68	0.72	0.29	0.59	0.23	nd	0.48
928/bulk	42.1	50.0	2.28	0.12	0.07	0.58	4.29	0.08	0.05	0.37	nd	0.47
935A/Fe	32.6	64.1	1.00	0.11	0.06	0.71	1.18	0.08	0.05	0.14	nd	0.50
935B/Si	69.3	26.3	1.12	0.07	0.05	0.84	1.84	0.12	0.05	0.24	nd	0.44
935C/Fe	27.1	70.0	0.57	0.10	0.07	0.60	1.34	0.05	0.04	0.18	nd	0.52
935D/Si	63.6	29.5	2.15	0.10	0.06	1.00	2.71	0.17	0.09	0.57	0.02	0.47
935E/Fe	23.8	74.6	0.12	0.08	0.06	0.36	0.70	0.02	0.03	0.21	nd	0.51
935F/Si	64.0	32.8	0.73	0.05	0.04	0.75	1.20	0.07	0.04	0.30	nd	0.42
935G/Fe	36.2	61.6	0.38	0.07	0.05	0.52	0.88	0.05	0.03	0.23	nd	0.49
935H/Si	66.7	29.4	0.67	0.05	0.05	0.99	1.59	0.08	0.04	0.40	nd	0.42
935I/Fe	27.8	69.9	0.27	0.07	0.06	0.81	0.88	0.04	0.03	0.12	nd	0.51
935J/Si	58.1	33.9	2.87	0.12	0.08	1.78	2.46	0.23	0.11	0.30	nd	0.49

$Fe_2O_3t = Fe_2O_3$ as total Fe, $Fe^{2+}/\Sigma Fe = Fe^{2+}/Fe^{2+} + Fe^{3+}$, Si = silica-rich bands, Si + Al = silica + alumina rich bands, im = intermediate (silica + Fe-rich bands), Fe = Fe-rich bands, bulk = analysed as bulk-rock, nd = not detectable.

Table 4B
Selected trace elements of the Itilliarsuk BIF. Samples are presented with the last three digits only.

Sample	902A	902B	902C	902D	902E	902F	902G	902H	926	935A	935B	935C	935D	935E	935F	935G	935H	935I	935J
	Si+Al	Si+Al	Im	Si+Al	Si+Al	Im	Im+Al	Im	Bulk	Fe	Si	Fe	Si	Fe	Si	Fe	Si	Fe	Si
ICP-MS (ppm)																			
Sc	9.79	7.57	7.56	11.6	9.88	6.47	3.62	4.05	4.36	3.12	4.21	3.77	0.91	nd	5.03	2.45	3.23	1.98	10.2
Cr	56.4	46.7	39.9	51.9	57.1	33.1	47.3	9.15	17.5	25.2	13.6	12.5	2.48	3.29	9.68	11.0	10.5	7.98	20.5
Ni	30.3	32.6	29.1	34.4	25.9	20.8	18.7	7.17	20.5	17.0	8.03	15.0	1.21	6.21	6.13	10.9	6.51	20.0	19.3
Rb	8.02	4.39	0.74	15.7	5.41	1.25	3.72	0.66	10.9	0.30	0.28	0.82	0.06	0.35	0.62	0.75	0.56	1.01	3.25
Sr	215	191	58.1	316	371	57.5	279	22.2	24.3	7.08	16.0	14.0	3.27	7.25	12.1	6.57	11.1	4.28	4.42
Y	1.79	2.72	7.20	2.00	1.45	8.30	1.89	3.99	3.87	4.84	2.53	3.79	1.06	2.79	2.46	1.12	2.33	3.66	4.23
Zr	77.9	51.4	67.1	63.9	87.9	22.0	66.3	4.57	14.5	18.1	11.2	15.0	1.98	7.27	8.07	10.8	8.39	11.6	14.9
Hf	2.13	1.47	1.59	2.20	2.48	0.58	1.76	0.13	0.40	0.46	0.29	0.38	0.06	0.18	0.21	0.27	0.23	0.28	0.45
Pb	7.00	6.18	2.26	9.90	8.95	1.65	7.48	1.64	1.34	0.47	0.90	0.50	0.15	0.24	0.72	0.44	0.57	0.28	0.47
Th	0.55	1.65	1.47	0.82	0.76	1.15	0.75	0.36	0.36	0.44	0.15	0.16	0.05	0.08	0.08	0.04	0.04	0.18	0.31
U	0.63	0.47	0.54	0.52	0.43	0.57	0.76	0.21	0.26	0.24	0.16	0.20	0.06	0.14	0.22	0.23	0.22	0.16	0.11
La	2.12	3.30	5.17	2.13	2.62	13.01	3.94	1.14	4.07	4.29	2.91	3.51	1.14	2.49	1.76	0.69	1.79	1.78	3.74
Ce	7.85	11.4	20.2	8.61	7.41	23.6	10.6	2.48	14.8	11.3	8.21	5.78	2.13	4.01	6.23	6.36	4.27	4.88	8.54
Pr	0.45	0.97	1.49	0.65	0.66	3.24	0.76	0.28	0.93	1.24	0.63	0.73	0.24	0.54	0.38	0.16	0.43	0.48	1.03
Nd	1.74	3.80	5.92	2.53	2.61	12.66	2.89	1.16	3.68	5.04	2.52	3.12	0.96	2.23	1.61	0.66	1.84	2.07	4.41
Sm	0.33	0.75	1.29	0.47	0.46	2.29	0.48	0.25	0.73	1.07	0.46	0.72	0.19	0.46	0.35	0.17	0.41	0.52	0.99
Eu	0.10	0.24	0.42	0.17	0.14	0.71	0.17	0.10	0.21	0.34	0.17	0.24	0.08	0.15	0.15	0.06	0.16	0.16	0.37
Gd	0.14	0.32	0.57	0.20	0.19	0.97	0.20	0.13	0.33	0.48	0.21	0.32	0.09	0.20	0.16	0.08	0.19	0.25	0.44
Tb	0.05	0.11	0.21	0.07	0.05	0.31	0.07	0.07	0.13	0.18	0.08	0.13	0.03	0.08	0.07	0.04	0.08	0.11	0.16
Dy	0.32	0.67	1.33	0.42	0.29	1.72	0.37	0.52	0.72	1.00	0.49	0.72	0.20	0.43	0.44	0.20	0.46	0.68	0.93
Ho	0.07	0.14	0.27	0.09	0.06	0.31	0.07	0.13	0.14	0.19	0.09	0.13	0.04	0.08	0.09	0.04	0.09	0.13	0.18
Er	0.24	0.41	0.82	0.26	0.17	0.87	0.21	0.37	0.35	0.53	0.27	0.34	0.11	0.23	0.24	0.10	0.25	0.36	0.48
Tm	0.04	0.06	0.12	0.04	0.02	0.11	0.03	0.05	0.04	0.07	0.03	0.04	0.01	0.03	0.03	0.01	0.03	0.05	0.06
Yb	0.27	0.36	0.78	0.26	0.17	0.71	0.20	0.35	0.27	0.46	0.24	0.28	0.09	0.21	0.20	0.09	0.18	0.32	0.38
Lu	0.04	0.05	0.12	0.04	0.03	0.11	0.03	0.06	0.04	0.07	0.04	0.04	0.01	0.03	0.03	0.01	0.03	0.05	0.06
ΣREY	15.6	25.3	45.9	17.9	16.4	68.9	21.9	11.1	30.3	31.1	18.9	19.9	6.4	14.0	14.2	9.8	12.6	15.5	26.0
Y/Ho	24.3	20.1	26.3	22.9	25.6	26.9	26.1	31.4	28.5	25.4	27.1	29.9	27.7	34.1	28.0	30.0	25.5	27.2	23.4
[La/La*]PAAS	1.26	0.98	1.02	0.94	1.15	1.14	1.39	1.38	1.28	1.08	1.44	1.82	1.47	1.53	1.61	1.31	1.53	1.49	1.39
[Ce/Ce*]PAAS	2.06	1.44	1.68	1.63	1.38	0.89	1.66	1.17	1.96	1.16	1.66	1.09	1.13	0.97	2.17	4.93	1.34	1.43	1.15
[Eu/Eu*]PAAS	1.52	1.59	1.58	1.77	1.65	1.58	1.77	1.58	1.35	1.52	1.69	1.57	1.94	1.53	1.86	1.56	1.78	1.30	1.81
[Pr/Yb]PAAS	0.53	0.84	0.60	0.79	1.21	1.43	1.19	0.25	1.08	0.85	0.83	0.83	0.84	0.80	0.59	0.56	0.74	0.47	0.85
[Sm/Yb]PAAS	0.61	1.05	0.82	0.90	1.34	1.61	1.20	0.35	1.35	1.17	0.98	1.30	1.09	1.08	0.86	0.91	1.11	0.81	1.30

La/La* = [La/(3Pr − 2Nd)]PAAS, Ce/Ce* = [Ce/(2Pr − 1Nd)]PAAS, Eu/Eu* = [Eu/(0.67Sm + 0.33Tb)]PAAS.
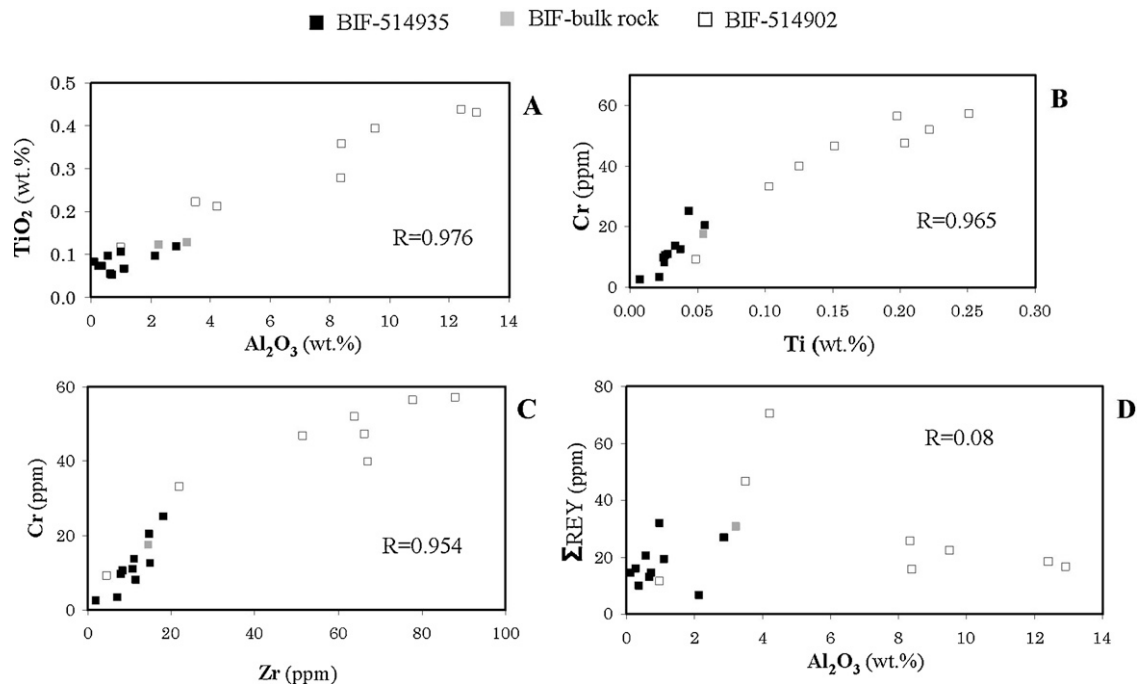
Fig. 9. Correlation diagrams between the most immobile and insoluble elements in the Itilliarsuk BIF. (A, B, C) represents strong positive correlation between different immobile and insoluble elements in the Itilliarsuk BIF. Sample 514935 contains lower concentration of these elements relative to sample 514902. (D) shows decoupling of the REY from the alumina-content.
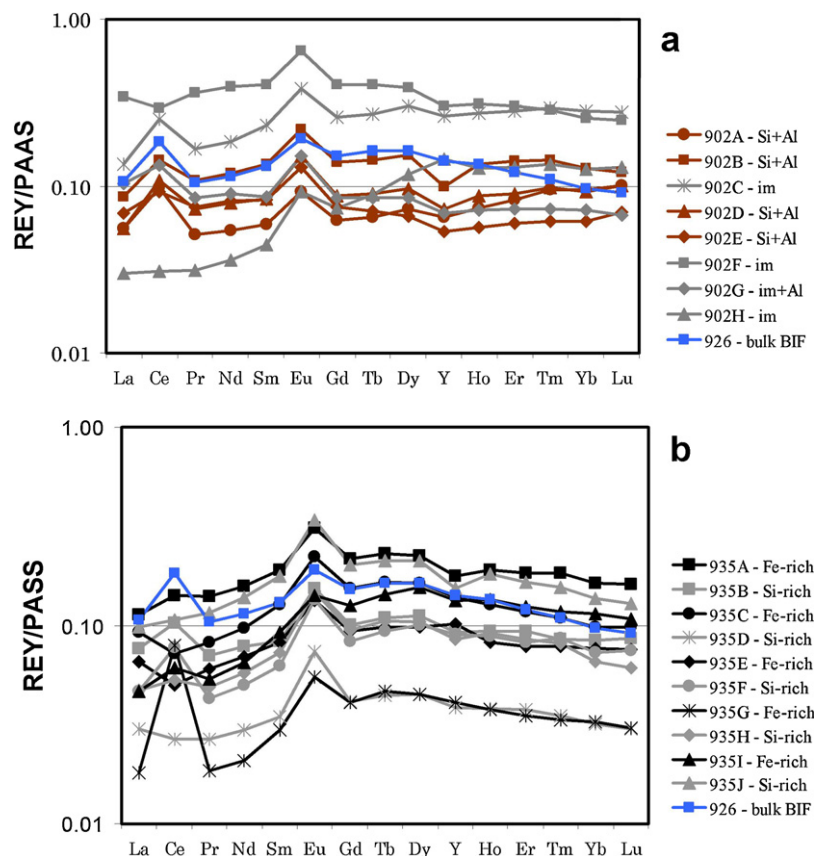

Fig. 10. PAAS-normalised REY patterns of the Itilliarsuk BIF. (a) Shows the eight mesobands separated from sample 514902. Three of these bands, 514902E, 514902F and 514902G, have enriched LREE relative to HREE pattern. Note that band H shows LREE « HREE and therefore has a completely different REY pattern than the seven neighbouring bands. (b) Displays the bands separated from sample 514935 – the most chemically pure of the BIF samples. All 10 bands have LREE < HREE. Insert in both graphs is the bulk-BIF sample 514926. See Section 5.2.1 for further details.

Table 5
Major and selected trace elements of the associated lithologies at Itilliarsuup Qaqqaa.

	Felsic schist				Qz–Bi–Gn schist		Stau. schist	Gn–Bi schist	Metagabbro				TTG
Sample	514910	514922	514925	514927	514909	514931	514914	514916	514903	514904	514907	514917	514934
XRF (wt.%)													
SiO_2	68	68	67	68	59	61	62	55	47	50	56	49	71
TiO_2	0.36	0.38	0.37	0.38	0.40	0.47	0.84	0.82	1.07	1.06	1.10	0.76	0.19
Al_2O_3	15.3	16.1	14.2	15.6	16.4	15.7	20.7	19.4	13.6	12.1	15.0	13.5	16.5
Fe_2O_3t	5.7	5.5	8.3	6.4	11.8	11.3	6.8	11.6	17.6	15.9	12.0	11.8	2.3
MnO	0.03	0.03	0.04	0.05	0.04	0.05	0.04	0.08	0.23	0.18	0.15	0.23	0.02
MgO	1.54	1.85	2.20	1.30	3.15	2.34	2.56	2.73	5.96	9.51	4.56	9.77	0.67
CaO	3.08	2.18	3.49	3.25	2.34	2.64	0.76	3.33	11.9	9.43	7.05	13.6	3.05
Na_2O	4.77	4.78	2.51	3.06	4.72	4.30	3.09	4.64	2.35	2.02	3.86	0.50	4.90
K_2O	0.80	1.43	1.61	1.42	2.42	1.85	2.92	1.79	0.15	0.11	0.62	0.20	1.30
P_2O_5	0.05	0.04	0.05	0.05	0.20	0.09	0.05	0.10	0.13	0.06	0.09	0.06	0.05
S	0.07	0.06	0.14	0.09	nd	nd	0.03	nd	0.03	nd	0.07	0.07	nd
Al_2O_3/TiO_2	42	42	38	42	41	33	25	24	13	12	14	18	89
SiO_2/Al_2O_3	4.5	4.2	4.7	4.4	3.6	3.9	3.0	2.9	–	–	–	–	4.3
ICP-MS (ppm)													
Sc	16.6	18.6	11.7	7.8	19.1	18.2	22.2	29.2	24.1	25.8	41.1	20.3	14.9
Ti	2398	2280	2132	2242	2403	2835	4886	4931	7650	7029	7809	5445	1159
V	40.4	47.6	45.7	44.1	44.4	79.7	174	175	346	327	356	275	13.9
Cr	23.0	29.8	31.8	22.8	34.8	51.9	143	193	296	271	306	284	2.62
Ni	12.8	19.9	18.1	12.2	33.5	33.4	76.0	85.0	159	137	138	161	3.09
Rb	13.6	25.7	21.0	21.3	29.7	31.3	24.5	22.3	0.18	0.05	5.98	0.04	12.9
Sr	166	188	164	191	109	96.9	45.5	188	44.2	35.8	81.7	24.0	228
Y	2.08	1.58	1.08	2.04	2.46	2.60	3.49	4.54	3.11	3.85	4.90	4.70	0.89
Zr	76.4	84.8	68.9	88.9	150	91.4	139	131	40.1	56.2	67.7	18.8	69.0
Nb	2.73	2.93	2.62	2.58	4.34	3.58	6.21	6.47	3.03	2.82	3.16	2.07	2.05
Ba	134	172	277	134	202	120	360	178	41.1	4.32	88.2	11.2	332
Hf	2.11	2.26	1.74	2.30	4.27	2.60	3.96	3.75	1.19	1.66	1.96	0.67	2.00
Ta	0.22	0.25	0.21	0.22	0.37	0.33	0.57	0.60	0.42	0.69	0.40	0.48	0.08
Pb	3.07	5.29	8.20	6.54	4.83	3.76	8.78	13.6	3.13	2.36	3.79	3.63	6.07
Th	0.66	0.86	0.40	1.20	1.03	0.88	1.56	1.33	0.05	0.07	0.07	0.03	1.44
U	0.67	0.83	0.57	0.53	1.41	0.87	1.07	1.48	0.09	0.10	0.10	0.07	0.12
La	7.24	4.41	3.10	5.60	5.31	4.85	1.58	6.18	0.79	1.13	1.90	1.04	5.94
Ce	19.0	12.3	8.82	16.1	16.4	14.2	5.76	19.0	1.64	3.47	4.51	3.18	13.1
Pr	1.65	1.19	0.79	1.52	1.42	1.32	0.61	1.74	0.30	0.44	0.69	0.42	1.52
Nd	6.09	4.62	2.98	5.75	5.42	5.11	2.60	6.87	1.61	2.31	3.49	2.31	5.64
Sm	0.99	0.79	0.51	1.01	0.97	0.93	0.59	1.28	0.49	0.68	1.05	0.73	0.96
Eu	0.34	0.31	0.17	0.37	0.40	0.32	0.24	0.53	0.23	0.28	0.45	0.22	0.28
Gd	0.83	0.68	0.41	0.89	0.91	0.89	0.69	1.28	0.67	0.91	1.38	0.98	0.74
Tb	0.11	0.09	0.06	0.11	0.13	0.12	0.13	0.19	0.11	0.15	0.22	0.16	0.08
Dy	0.56	0.46	0.30	0.58	0.72	0.68	0.93	1.19	0.73	0.93	1.32	1.09	0.37
Ho	0.10	0.08	0.05	0.10	0.12	0.12	0.20	0.22	0.15	0.19	0.25	0.23	0.05
Er	0.28	0.24	0.16	0.29	0.34	0.35	0.58	0.65	0.43	0.53	0.65	0.67	0.13
Tm	0.04	0.03	0.02	0.04	0.04	0.04	0.09	0.09	0.06	0.08	0.08	0.09	0.01
Yb	0.24	0.22	0.15	0.26	0.28	0.31	0.59	0.61	0.41	0.49	0.51	0.63	0.08
Lu	0.04	0.04	0.02	0.04	0.04	0.05	0.08	0.09	0.06	0.08	0.08	0.09	0.01
ΣREE	37.5	25.4	17.5	32.7	32.5	29.3	14.7	39.9	7.7	11.7	16.6	11.8	29.0
$[La/Yb]_{CHON}$	20.9	13.8	14.1	14.7	13.0	10.9	1.9	7.0	1.4	1.6	2.6	1.1	49.0
$[Eu/Eu^*]_{CHON}$	1.11	1.27	1.09	1.17	1.27	1.07	1.08	1.25	1.24	1.11	1.18	0.83	0.99
Ti/V	–	–	–	–	–	–	–	–	22	21	22	20	–

the higher biotite content) and elevated Cr, Ni and Zr. The chondrite-normalised REE patterns show slightly lower La/Yb_{CHON} as a consequence of higher content of HREEs (Fig. 11).

5.1.4. Staurolite schist and garnet–biotite schist

These rocks record the same range in geochemistry with distinct characters such as low Al_2O_3/TiO_2 ratios (24), low SiO_2-content and high abundances of Al_2O_3 (~20 wt.%), TiO_2, Cr, Ni, V, Zr, Nb and Yb. Their chondrite-normalised REE trends show $[La/Yb]_{CHON} < 7$, with the staurolite schist having the weakest LREE enrichment of 1.9. Their HREE abundances are similar to the metagabbros (Fig. 11).

5.1.5. Metagabbro

The total REE concentration ranges from 7.7 to 16.6 ppm, and the chondrite-normalised REE diagram shows element abundances between 3 and 7 times the chondrite values (Fig. 10). These REE values are generally low compare with other Mesoarchaean gabbros (see Rollinson, 1983; Wang et al., 2004; Polat et al., 2008). The very coarse-grained sample 514917 displays a fairly flat REE pattern ($[La/Yb]_{CHON} = 1.1$), while sample 514907 is enriched in LREEs ($[La/Yb]_{CHON} = 2.6$).

5.1.6. TTG-basement (orthogneiss)

The basement rock displays true geochemical characteristic of an Archaean TTG (tonalite–trondhjemite–granodiorite) suite with high content of SiO_2, Al_2O_3, Na_2O, Sr, and low content of TiO_2, Fe_2O_3, MgO, K_2O, transition metals, rubidium and Yb. The steep fractionated REE curve ($[La/Yb]_{CHON} = 49$) shows subchondritic HREEs (Fig. 11). In addition, the curve has no Eu-anomaly ($[Eu/Eu^*]_{CHON} = 0.99$), consistent with it being Archaean continental crust (Taylor and McLennan, 1985; Martin et al., 2005; Rollinson, 2007).
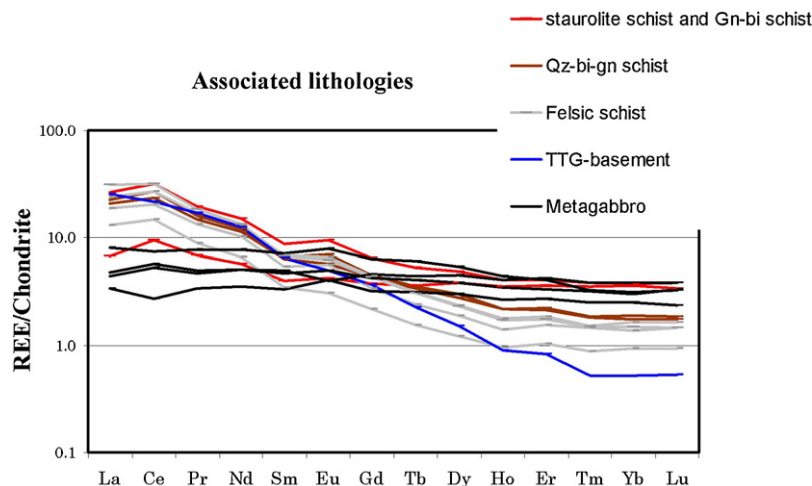
Fig. 11. Chondrite-normalised REE patterns of the associated lithologies of the Itilliarsuup Qaqqaa. The TTG-basement shows a very steep fractionated REE pattern with low HREE abundances. The different schist types show an increase in HREE from the felsic schist, the quartz–biotite–garnet schist and to the staurolite and Gn–Bi schist. In general, all the schists also display positive cerium-anomalies. The metagabbro, sample 514907, shows slightly LREE-enriched character relative to HREEs.

5.2. Isotopes

5.2.1. Pb isotopes

Whole-rock Pb isotopes for individual BIF bands, bulk-BIF and selected associated lithologies from the Itilliarsuup Qaqqaa are listed in Table 6. The uranogenic common Pb isotope diagram is plotted in Fig. 12A, and the uranogenic vs. thorogenic common Pb isotope diagram is shown in Fig. 12B. The Stacey and Kramers (1975) growth curve for average crustal Pb evolution is shown for comparison. In Fig. 12A, the slope of the well-defined regression line $[(^{235}U/^{238}U) \times e^{\lambda 235t} - 1/e^{\lambda 238t} - 1]$ corresponds to an age of

1895 ± 48 Ma (MSWD = 30). This age is relatively consistent with the age (1750–1925 Ma) obtained by Rasmussen and Holm (1999) in the eastern Nuussuaq for the early Proterozoic Rinkian orogenic event. When including the basement gneiss and the presumably younger acidic metavolcanic in the regression (not shown), the scatter and the age increases (2083 ± 150 Ma, MSWD = 481), probably as a result of incomplete resetting or due to the fact that the rocks are genetically unrelated from the other rocks at Itilliarsuup Qaqqaa. The model age defined by the intersection of the growth curve is 2631 Ma. Apparently, this age is too young to represent the extraction age from involved sources and is the result of the

Table 6
Pb isotope data of the Itilliarsuk BIF and selected associated lithologies.

Sample	$^{206}Pb/^{204}Pb$	$\pm 2\sigma^*$	$^{207}Pb/^{204}Pb$	$\pm 2\sigma^*$	$^{208}Pb/^{204}Pb$	$\pm 2\sigma^*$	r_1 [a]	r_2 [b]
BIF								
514902A (Si + Al)	16.996	0.009	15.153	0.010	36.589	0.029	0.959	0.929
514902B (Si + Al)	16.570	0.009	15.077	0.010	36.612	0.028	0.966	0.931
514902C (im)	19.620	0.010	15.423	0.010	38.516	0.030	0.966	0.937
514902D (Si + Al)	16.142	0.011	15.028	0.012	36.323	0.032	0.964	0.940
514902E (Si + Al)	16.255	0.009	15.048	0.010	36.898	0.029	0.968	0.934
514902F (im)	20.962	0.026	15.590	0.021	39.190	0.070	0.921	0.736
514902G (im + Al)	16.627	0.009	15.098	0.010	36.229	0.031	0.937	0.847
514902H (im)	20.193	0.010	15.522	0.010	41.969	0.032	0.970	0.937
514926 (bulk-BIF)	17.978	0.030	15.230	0.026	37.874	0.068	0.982	0.958
514928 (bulk-BIF)	18.893	0.023	15.394	0.020	37.920	0.052	0.981	0.964
514935A (Fe)	25.692	0.047	16.190	0.031	43.288	0.084	0.986	0.980
514935C (Fe)	26.584	0.071	16.254	0.044	41.113	0.113	0.990	0.989
514935D (Si)	16.850	0.012	15.042	0.012	36.664	0.032	0.971	0.940
514935E (Fe)	28.605	0.051	16.468	0.030	41.779	0.081	0.976	0.943
514935F (Si)	24.978	0.027	16.087	0.018	41.847	0.051	0.983	0.958
514935G (Fe)	23.974	0.029	15.923	0.020	39.860	0.054	0.980	0.952
514935H (si)	23.627	0.020	15.894	0.015	40.407	0.041	0.973	0.946
514935I (Fe)	23.641	0.037	15.865	0.026	41.630	0.069	0.974	0.973
514935J (Si)	21.524	0.033	15.655	0.025	42.053	0.070	0.974	0.973
Assoc. rocks								
514903/metagabbro	15.841	0.023	15.047	0.023	35.586	0.056	0.982	0.972
514904/metagabbro	15.919	0.011	15.040	0.012	35.355	0.031	0.971	0.936
514907/metagabbro	15.460	0.017	14.958	0.017	35.214	0.043	0.980	0.959
514917/metagabbro	15.266	0.008	14.918	0.009	34.876	0.027	0.956	0.921
514914/staurolite schist	18.328	0.013	15.250	0.012	38.385	0.034	0.971	0.933
514920/sericite schist	15.052	0.008	14.841	0.009	34.645	0.026	0.966	0.935
514927/felsic schist	28.970	0.026	16.463	0.016	42.342	0.046	0.975	0.952
514933/acidic metavolcanic	26.309	0.014	16.716	0.011	44.207	0.036	0.959	0.905
514934/TTG-basement	13.396	0.012	14.301	0.014	36.944	0.039	0.966	0.940

* Errors are two standard deviations absolute (Ludwig, 2005).
[a] Error correlation (r_1) on $^{206}Pb/^{204}Pb$ vs. $^{207}Pb/^{204}Pb$ (Ludwig, 2005).
[b] Error correlation (r_2) on $^{206}Pb/^{204}Pb$ vs. $^{208}Pb/^{204}Pb$ (Ludwig, 2005).
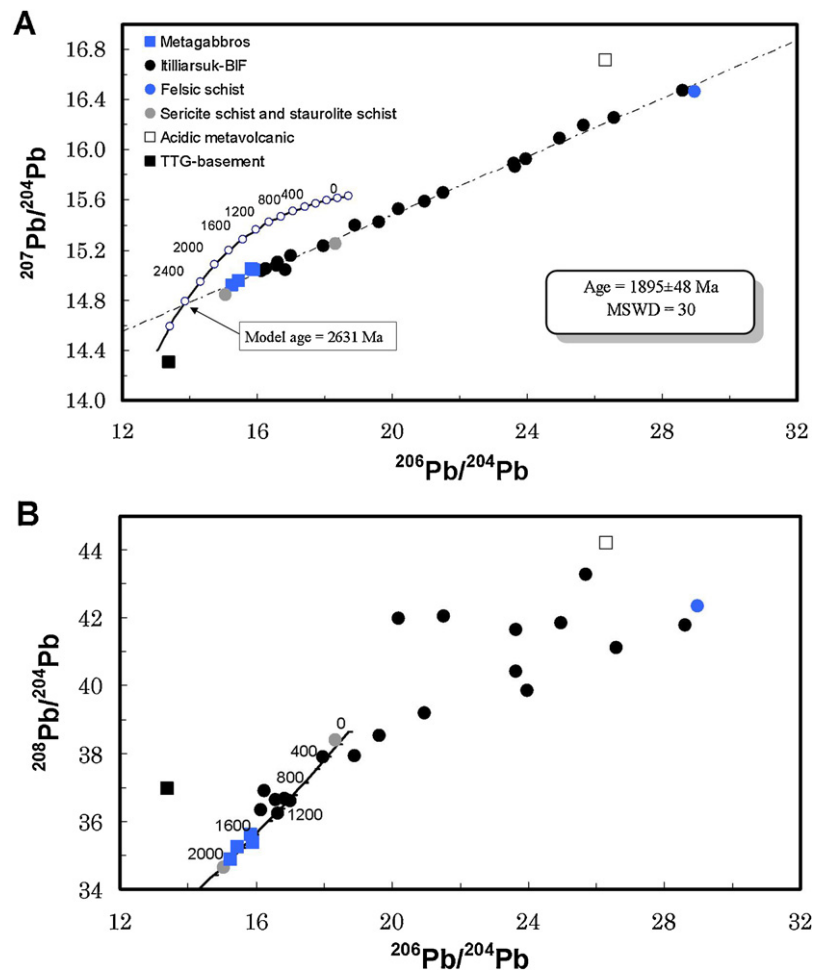
Fig. 12. (A) Uranogenic common Pb isotope diagram of the samples studied herein. Except for the acidic metavolcanic and the TTG-basement all samples plot along a well-defined correlation line with a slope corresponding to an age of 1895 ± 48 Ma (MSWD = 30). This age is compatible with the Rinkian orogeny. The intersection with the Stacey and Kramers (1975) growth curve represents too young a model age (2631 Ma) as a consequence of the metamorphic resetting of the system. In (B) the same samples are plotted in the thorogenic vs. uranogenic common Pb isotope diagram. High scatter of large part of the BIF samples is obvious. These samples, together with the felsic schist and the acidic metavolcanic, are very radiogenic, whereas six of the BIF samples and the TTG-basement evolved with high Th/U ratios (plots left of the Stacey and Kramers growth curve).

re-equilibration of the U–Pb system. Data points for the chemical pure BIF (sample 514935) plots at elevated, more radiogenic $^{207}Pb/^{204}Pb$ and $^{206}Pb/^{204}Pb$ values than the chemical impure BIF (sample 514902) (see Table 6 for exact values).

The uranogenic vs. thorogenic common Pb-diagram (Fig. 12B) shows excessive scatter, and enriched $^{206}Pb/^{204}Pb$ relative to $^{208}Pb/^{204}Pb$ values (scattered and low $^{232}Th/^{238}U$) for the chemical pure sample 514935. However, uniform $^{206}Pb/^{204}Pb$ and $^{208}Pb/^{204}Pb$ values are found in six of the BIF bands and some of these, including the TTG-basement, have slightly elevated $^{208}Pb/^{204}Pb$ relative to $^{206}Pb/^{204}Pb$ (plotting left of the growth curve) suggesting derivation from high κ ($^{232}Th/^{238}U$) source(s).

5.2.2. Sm–Nd isotopes

Table 7 displays whole-rock Sm–Nd isotope systematics of the Itilliarsuk BIF samples and selected associated lithologies. Four mesobands were rejected from sample 514902: samples 514902C and 514902D due to poor analytical statistics on the $^{143}Nd/^{144}Nd$ measurement, and samples 514902E and 514902F due to possible open system behaviour of the Sm–Nd system. The latter is reflected in high positive $\varepsilon_{Nd}(i)$ (+12.4 and +8.3) and hence too low T_{DM} ages (2.34 and 2.55 Ga) to be geologically meaningful. Similarly, the analysis of the bulk-BIF (sample 514926) was rejected due to a T_{DM} age of 2.81 Ga.

The four mesobands from sample 514902 display a high spread in their $\varepsilon_{Nd}(i)$ values. Bands A and G have positive $\varepsilon_{Nd}(i)$ values of +3.05 and +3.01 and T_{DM} ages of 2.93 and 2.94 Ga, respectively, whilst band B and the intermediate band H record negative $\varepsilon_{Nd}(i)$ values of −0.56 and −0.95, corresponding to T_{DM} ages of 3.23 and 3.32 Ga, respectively. The three mesobands (Lok83-A, Lok83-B and Lok83-C) show similar Nd isotopic trends as the two mesobands A and G in sample 514902 with a $\varepsilon_{Nd}(i)$ range of +2.37 to +3.75, and T_{DM} ages of 3.00–2.88 Ga. Interestingly, sample 514935 reveals systematic variations between the silica- and Fe-rich bands. All $\varepsilon_{Nd}(i)$ for the silica bands are characterised by positive values with an average of +1.35 and T_{DM} ages from 3.23 to 2.85 Ga. In contrast, lower and mostly subchondritic values of $\varepsilon_{Nd}(i)$ and, hence, old T_{DM} ages, characterise the five iron-rich bands ($\varepsilon_{Nd}(i) = −2.87$ to +0.09, average of −1.29, and T_{DM} ages = 3.61–3.22 Ga, average of 3.4 Ga). The associated lithologies are all characterised by positive $\varepsilon_{Nd}(i)$ values. The felsic schist, the sericite schist and the staurolite schist all show very similar T_{DM} ages of 2.94, 2.91 and 2.93 Ga, respectively. Likewise, the acidic metavolcanic yields a T_{DM} age of 2.95 Ga which, apparently, is too old considering the U–Pb zircon age of 2847 ± 4 Ma (Connelly et al., 2006). Furthermore, the presumably older TTG-basement records a T_{DM} age of 3.05 Ga, which predates the above ages except those BIF-bands with negative $\varepsilon_{Nd}(i)$ values.

Table 7
Sm–Nd isotopic data of the Itilliarsuk BIF and selected associated lithologies.

Sample	Sm (ppm)	Nd (ppm)	$^{147}Sm/^{144}Nd$	$^{143}Nd/^{144}Nd$	$\pm2\sigma$ abs.	T_{DM}*	$\varepsilon_{Nd}(0)$	$\varepsilon_{Nd}(2847\,Ma)$
BIF								
514902A (Si + Al)	0.57	3.24	0.10710	0.511109	62	2.93	−29.82	3.05
514902B (Si + Al)	0.69	3.50	0.11906	0.511150	5	3.23	−29.02	−0.56
514902C (im)	1.06	4.79	0.13403	0.511531	311	3.11	−21.59	1.40
514902D (Si + Al)	0.71	3.74	0.11407	0.511266	105	2.89	−26.77	3.55
514902E (Si + Al)	1.18	8.22	0.08703	0.511210	8	2.34	−27.86	12.44
514902F (im)	2.10	11.96	0.10601	0.511355	7	2.55	−25.03	8.27
514902G (im + Al)	1.43	7.78	0.11139	0.511188	7	2.94	−28.29	3.01
514902H (im)	0.19	0.89	0.13000	0.511336	87	3.32	−25.39	−0.95
514926 bulk-BIF	1.08	6.21	0.10489	0.511149	6	2.81	−29.04	4.65
514928 bulk-BIF	1.31	6.04	0.13161	0.511443	5	3.18	−23.31	0.55
514935A (Fe)	0.91	4.20	0.13097	0.511407	7	3.22	−24.01	0.09
514935B (Si)	1.11	5.48	0.12237	0.511447	19	2.85	−23.23	4.05
514935C (Fe)	0.78	3.39	0.14005	0.511531	60	3.36	−21.59	−0.83
514935D (Si)	1.40	6.26	0.13550	0.511512	8	3.21	−21.97	0.47
514935E (Fe)	0.71	3.25	0.13288	0.511420	6	3.28	−23.75	−0.36
514935 F (Si)	0.88	3.94	0.13464	0.511525	6	3.14	−21.71	1.05
514935G (Fe)	0.79	3.42	0.14047	0.511454	10	3.54	−23.09	−2.50
514935H (si)	1.10	4.88	0.13644	0.511543	11	3.18	−21.36	0.74
514935I (Fe)	0.54	2.31	0.14283	0.511479	24	3.61	−22.60	−2.87
514935J (Si)	1.24	5.37	0.13934	0.511582	7	3.23	−20.60	0.43
Lok83-A[#]	0.79	4.12	0.11620	0.511292	7	2.92	−26.25	3.29
Lok83-B[#]	1.82	10.00	0.11034	0.511206	6	2.88	−27.94	3.75
Lok83-C[#]	1.36	6.79	0.12073	0.511331	6	3.00	−25.50	2.37
Assoc. rocks								
514903/metagabbro	2.24	6.64	0.20398	0.512982	7	2.64	6.71	4.07
514904/metagabbro	2.12	6.37	0.20174	0.512924	6	2.89	5.58	3.76
514907/metagabbro	2.94	8.80	0.20253	0.512897	5	3.46	5.05	2.94
514917/metagabbro	1.86	5.40	0.20797	0.513032	5	3.14	7.69	3.59
514914/staurolite schist	4.45	25.11	0.10718	0.511108	6	2.93	−29.85	3.00
514920/sericite schist	0.66	3.32	0.11982	0.511364	7	2.91	−24.85	3.36
514927/felsic schist	2.09	12.48	0.10157	0.510996	6	2.94	−32.04	2.86
514933/acidic metavolcanic	3.00	17.38	0.10432	0.511042	5	2.95	−31.14	2.75
514934/TTG-basement	1.59	9.84	0.09788	0.510842	5	3.05	−35.04	1.19

* Refers to the depleted mantle model age by DePaolo (1981).
# Three samples provided by Nunaoil in 1996, and subsequently analysed by Robert Frei.

6. Discussion

6.1. Secondary alteration and Pb isotopes

When making geochemical interpretations of metamorphic rocks it is important to determine whether they have retained their primary geochemical signatures or whether they instead reflect secondary processes related to the metamorphic event. The amphibolite-facies metamorphism during the Rinkian orogeny resulted in resetting of the U–Pb system for the Itilliarsuup Qaqqaa sequence. If the internal differences in Pb isotope composition for the Itilliarsuk BIF reflect primary depositional signatures, then sample 514935 evolved with high-μ ($^{238}U/^{204}Pb$) from the time of deposition ($\geq2847\,Ma$) and onwards to the metamorphic event ($\sim1900\,Ma$). On the other hand, lower or higher $^{206}Pb/^{204}Pb$ values could also be attributed to loss or gain of uranium during the Rinkian tectono-metamorphic event, which seems the more likely. In the uranogenic vs. thorogenic common Pb-diagram, the bands from sample 514935 show extensive scatter and are enriched in $^{206}Pb/^{204}Pb$ relative to $^{208}Pb/^{204}Pb$ (low $^{232}Th/^{238}U$). This could imply: (1) that the bands evolved with high but rather heterogeneous Th/U ratios since the tectono-metamorphic event ($1895\pm48\,Ma$), which means that the metamorphic event disturbed the Th–U system of the mesobands to varying degrees (resulting in incomplete resetting of the Th–U system); or (2) the non-uniform Th/U ratios reflect a primary character by contribution from sources with variable Th/U signatures. When taking into account the relatively high-grade thermo-tectonic history for the rocks, the high scatter in sample 514935 most likely reflects later perturbation during the Rinkian orogeny. Th/U phases may also have been introduced to the system by metamorphic fluids as

suggested by Rosing and Frei (2004) on metasediments from the Isua area, SW Greenland.

6.2. Secondary alteration and REY

Although the REY are generally regarded as being immobile during most geological processes, there is a potential risk of secondary mobilisation, especially if the water to rock ratio was high during the metamorphism. As a result any initial differences in REY contents between individual bands would tend to be minimised (Bau, 1993; Bau and Dulski, 1996; Alexander et al., 2008). Therefore, the large differences observed in REY patterns and abundances between band H and the neighbouring bands in sample 514902 suggest that the metamorphic event did not significantly affect the REYs. The same is indicated by variable REY abundances in the chemical pure BIF (sample 514935). This view implies that the lack of correlation between REY and concentrations of Al_2O_3, TiO_2, Zr and the transition elements (Fig. 9D) is likely a result of the majority of the REYs being in solution prior to deposition and hence, they mirror seawater composition. On the other hand, the decoupling could also support that the REYs were hosted and deposited with the fine-grained clay detritus, but were disturbed and mobilised after the BIF deposition.

A positive Ce-anomaly is common in the Itilliarsuk BIF samples and this is generally not considered a normal feature of chemical sediments precipitated from Archaean seawater (Bolhar et al., 2004). Therefore, it is likely that a secondary process was responsible for accumulating cerium relative to neighbouring REEs. Frei et al. (2008) have previously reported such a process in Palaeoproterozoic iron formations from the Black Hills, South Dakota (USA). Those authors suggested that the most plausible explanation was

oxidative supergene enrichment of cerium during transport. This would tend to stabilise Ce^{4+} compounds relative to neighbouring LREE. The positive Ce-anomaly also occurs in the various schists in the Itilliarsuup Qaqqaa sequence indicating that the Ce-anomaly is independent of lithology and therefore of secondary origin.

6.3. Source characteristics

6.3.1. Terrigenous and seawater input

The seven mesobands (A–G) in sample 514902 contain signatures of terrigenous input, as reflected by the high modal content of biotite, and high but variable concentrations of Al_2O_3, HFSEs and the transition metals. High abundances of these elements in the Itilliarsuk BIF suggest weathering of both felsic and mafic (bimodal) sources. In addition, the strong correlations between Al_2O_3, HFSEs and the transition metals (Fig. 9A–C) indicate that the transition metals and HFSEs were likely hosted and deposited in the clay-rich fraction. Similarly, mixed chemical and terrigenous parentage is reported from the 3.8 Ga old Isua BIF, SW Greenland (Nutman, 1986) and from the ~3.8 Ga Nulliak-BIF, northern Labrador (Nutman et al., 1989). Also, Khan and Naqvi (1995) report mixed character within part of the BIF from the 3.0 to 2.6 Ga Dharwar Craton in India. This BIF here is enriched in Al_2O_3 (>2 wt.%), HFSE and transition metals, and as a consequence they defined the unit shaley-BIF. Likewise, parts of the north-eastern area of the Itilliarsuk BIF (Fig. 3), represented by the seven bands in sample 514902, can also be classified as shaley-BIF. The high Al-content is further documented by the often high amount of garnets developed within the BIF at these surroundings (Fig. 5E).

Although some samples indicate terrigenous input, some of the BIF layers are more chemically pure and thus reflective of seawater. For instance, Fig. 13 shows an average PAAS-normalised curve for four Itilliarsuk BIF bands from sample 514935 (red curve) and the chemically pure mesoband H from sample 514902 (grey curve).

These bands are the least altered (lack of Ce-anomalies) and are relatively poor in detrital alumina-silicates. They are, therefore, considered the most reliable proxies for the composition of the seawater from which they precipitated. As a comparison to the Itilliarsuk BIF, three other curves are shown in Fig. 13: REY concentrations of high-temperature (>350 °C) hydrothermal fluids from the Broken Spur vent site 29°N, Mid-Atlantic Ridge (Bau and Dulski, 1999); modern surface seawater from the South Pacific (Bolhar et al., 2004); the average of the top and bottom part of the succession from the 2.9 Ga Pongola BIF from South Africa (Alexander et al., 2008). As evident in the figure, the four bands from sample 514935 have compositions intermediate between that of high-temperature hydrothermal fluids (MREE enrichment relative to LREE and HREE, positive Eu-anomaly and chondritic Y/Ho ratio) and modern seawater (LREE depletion relative to HREE and positive La-anomaly). In this regard, we propose that the MREEs in the Itilliarsuk BIF were controlled by high-temperature hydrothermal fluids, whereas the HREEs were controlled by the bulk seawater. The REY pattern and abundances of the Pongola BIF are comparable to the Itilliarsuk BIF except for the higher MREE enrichment relative to the HREE and the relative higher Y-anomaly in the Pongola BIF. Alexander et al. (2008) suggested that the MREE enrichment in the Pongola BIF could also be a result of river transported Fe-colloidal particles which, in analogous to modern studies, are enriched in MREEs relative to LREEs and HREEs.

The composition of mesoband 514902H, on the other hand, appears to have been controlled primarily by bulk seawater as indicated by HREE » LREE, HREE > MREE and a positive, non-chondritic Y-anomaly (Y/Ho = 31). The absence of Ce-anomalies is in agreement with Archaean BIFs in general, and underscores that the oxidation level of the ambient seawater was too low for Ce(III) to oxidise to Ce(IV) and be removed via iron-oxyhydroxide precipitation. Evidence for superchondritic (>42) Y/Ho ratios in BIFs has been reported from the 3.7 Ga Isua BIF (Bolhar et al., 2004; Frei and
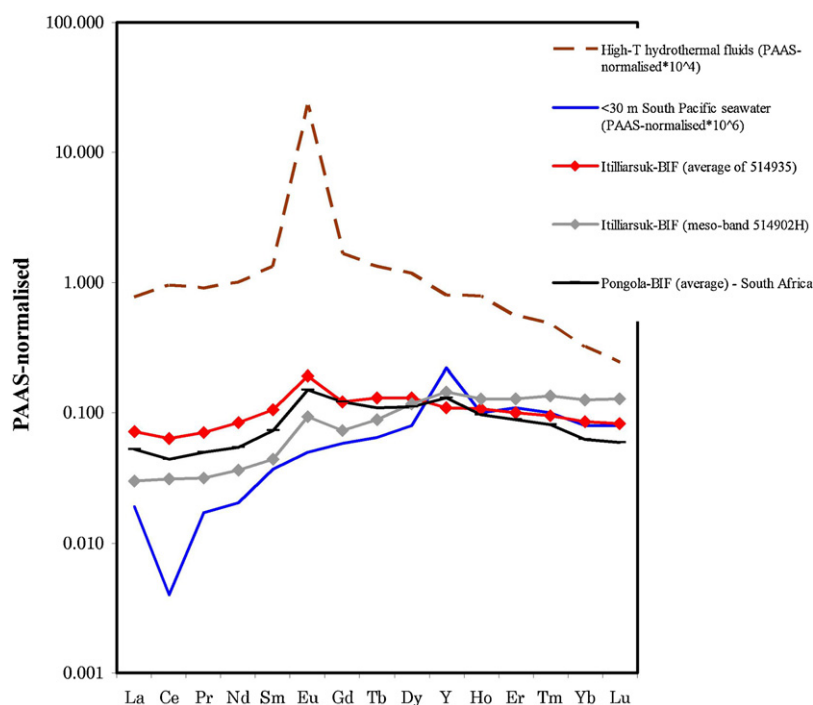

Fig. 13. PAAS-normalised REY patterns of the least altered and chemically pure bands from the Itilliarsuk BIF. The red curve represents the average of four bands from sample 514935, while the grey curve is the detritus-free band H from sample 514902. Also, plotted for comparison is: REY pattern (*10[4]) of modern high-T hydrothermal mid-Atlantic ridge fluids (Bau and Dulski, 1999); the REY pattern (*10[6]) of the average upper 30 m of South Pacific seawater (Bolhar et al., 2004); average BIF samples from the ~2.9 Ga Pongola BIF (Alexander et al., 2008). Both the Itilliarsuk BIF and the Pongola BIF are enriched in MREEs relative to LREEs and HREEs. See Section 6.3.1 for further explanations.(For interpretation of the references to color in this figure legend, the reader is referred to the web version of the article.)
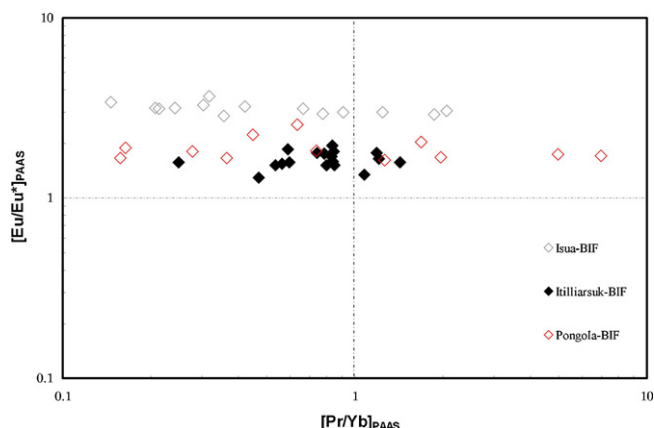
Fig. 14. PAAS-normalised Eu-anomalies and Pr/Yb ratios for the 3.7 Ga Isua BIF (Frei and Polat, 2007), the 2.9 Ga Pongola BIF (Alexander et al., 2008) and the Itilliarsuk BIF (this study). A large portion of the samples shows characteristic seawater LREE depletion relative to HREEs, and positive hydrothermal-derived Eu-anomalies. Note the higher magnitude in Eu-anomalies for the older Isua BIF.

Polat, 2007) and the 2.5 Ga Kuruman BIF (Bau and Dulski, 1996). In contrast, the Itilliarsuk BIF shows no specific elevated Y/Ho signature. This may suggest that the Y/Ho ratio in the seawater was suppressed by direct influx from hydrothermal "black smoker" vents and/or terrigenous sources with chondritic Y/Ho-ratios (~26).

PAAS-normalised Eu/Eu* and Pr/Yb for the Itilliarsuk BIF samples, the 2.9 Ga Pongola BIF and the older 3.7 Ga Isua BIF are plotted in Fig. 14. A positive Eu-anomaly and a general trend of LREE depletion relative to HREE are characteristic features of Archaean iron formations. Four of the shaley-BIF mesobands from sample 514902 show PAAS-normalised LREE enrichment (Pr/Yb > 1), which likely is a result of chemical sediments containing detrital components (Hofmann, 2005). However, in both the Itilliarsuk BIF and the

Pongola BIF the Eu-anomaly is less marked than the Isua BIF. According to Condie (1997) and Frei et al. (2008) this is consistent with the general trend of decreasing Eu/Eu* with decreasing age of Precambrian BIFs, as a consequence of the diminishing thermal and hydrothermal activities as the Earth cooled (e.g., De Wit and Hart, 1993; Arndt et al., 2008).

In terms of trace metal composition of the more chemically pure BIF layers, Ni shows concentrations typically ranging from 1.2 to 20 ppm. To put this into context, bulk rock Ni concentrations in various Archaean BIF range from 2.7 to 54 ppm in the 3.75 Ga old Isua BIF; 5–94 ppm in the 2.85 Ga old Yilgarn Block and Mount Gibson (Australia) and 10–46 ppm in the 2.75 Ga Carajas BIF (Brazil) (see Table S1 in Konhauser et al., 2009). The concentration of Ni is somewhat lower in the Itilliarsuk BIF. On-the-one-hand, the result is surprising because the oceans during the Eoarchean and Mesoarchean are believed to have been Ni-rich due to the abundant eruption of ultramafic lavas (e.g., komatiites) at that time (e.g., Arndt, 1991; Kamber et al., 2005). On-the-other-hand, and as discussed below, the BIF depositional basin was effected by bimodal volcanism with both mafic (e.g. tholeites) and, in particular, felsic (e.g., dacitic–rhyolitic) sources. This volcanism may have diluted the water column of Ni.

6.3.2. Neodymium isotopes and REY control

Fig. 15 displays a Sm–Nd isochron diagram, where the blue line characterises a well-defined regression line (MSWD = 0.94) through data points of shaley-BIF mesobands, the silica-band B (sample 514935), samples Lok-83A, Lok-83B and Lok-83C, the felsic schist, the sericite schist, the staurolite schist and the metagabbros. The slope matches an apparent age of 2889 ± 66 Ma and defines an initial ε_{Nd} of +3.7. Although there is potential risk of plotting such a composite Sm–Nd isochron diagram consisting of different lithologies, the lines do mirror a geologically meaningful age of the system as it predates the acidic metavolcanic (2847 ± 4 Ma) but postdate the TTG-basement (T_{DM} age = 3.05 Ga). Nevertheless, the Sm–Nd isotopic signals for the BIF samples at the blue line imply that
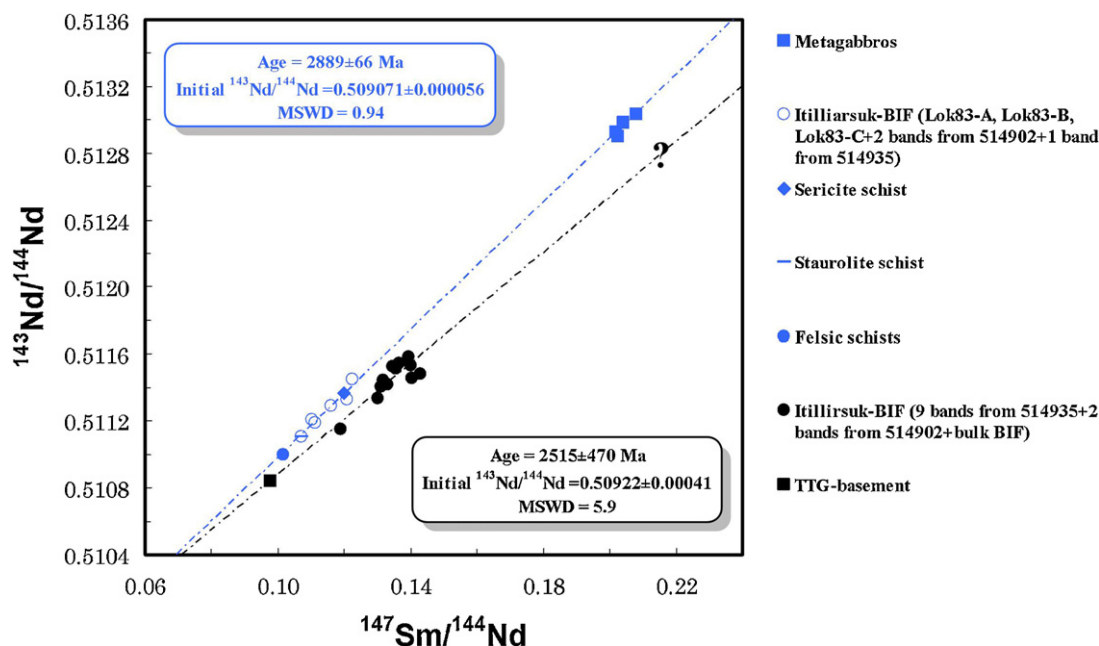

Fig. 15. Sm–Nd isochron diagram with data from the Itilliarsuk BIF and associated rocks at Itilliarsuup Qaqqaa. The blue line defines a correlation line with a slope corresponding to an apparent age of 2889 ± 66 Ma (MSWD = 0.94) and an initial ε_{Nd} value of +3.7. The REY in these BIF samples may have been controlled by mixing of the felsic schist and more mafic sources represented by the metagabbros. The slope of the black correlation line defines an apparent age of 2515 ± 470 Ma (MSWD = 5.9). This line has clearly no gechronological relevance but is rather a mixing line between the TTG-basement and an unknown enriched source (?). The iron-rich bands are all clustered around the black line hinting, that the Fe was derived from an enriched source. See Section 6.3.2 for further details. (For interpretation of the references to color in this figure legend, the reader is referred to the web version of the article.)

the REYs in the seawater were mainly governed by a mixture of the felsic schist, and more depleted mafic sources, reflected by the metagabbros. In contrast, the black data points refer to the four silica-rich and five Fe-rich bands (sample 514935), the mesobands B and H (sample 514902), the bulk-BIF (sample 514928) and the TTG-basement. The best fit through these BIF samples connect directly to the TTG-basement data point. Therefore, the black curve represents the errorchron (MSWD = 5.9) with a slope equivalent with an apparent age of 2515 ± 470 Ma and an initial ε_{Nd} value of −3. Clearly, this line has no geochronological meaning, and is thus, interpreted as being a mixing line. Those BIF samples plotting along the black mixing line suggest mixed REY affinities between the TTG-basement and an unknown (?) enriched source that presumably also supplied the iron to the Itilliarsuk BIF.

In sample 514935, the highest aluminium content is generally found in the silica-rich layers, which indicate a common source for both the silica and the detrital aluminium silicates. The low positive $\varepsilon_{Nd}(i)$ values for the silica-rich mesobands points to an origin of the silica from the depleted TTG-basement. The Al–$\varepsilon_{Nd}(i)$ relationship (Fig. 16a) reveals that the aluminium content is derived by sources with positive $\varepsilon_{Nd}(i)$ values. This relationship is in direct contrast to Alexander et al. (2009) for the 2.95 Ga old BIF from the Pietersburg greenstone belt (South Africa). Here, as for many Archaean BIFs, negative $\varepsilon_{Nd}(i)$ values are sourced from nearby old enriched continental crust, which, for the Pieterburg BIF, resulted in a negative Al–$\varepsilon_{Nd}(i)$ relationship.

The Fe–$\varepsilon_{Nd}(i)$ relationship is shown in Fig. 16b. As would be expected if the Fe was sourced from depleted MORB, the Fe-bands would contain positive $\varepsilon_{Nd}(i)$ values. However, this is not the case

for the Itilliarsuk BIF. Generally, subchondritic $\varepsilon_{Nd}(i)$ values are found for the Fe-bands and positive $\varepsilon_{Nd}(i)$ values are found within the silica-bands. From the 3.8 Ga Isua BIF, Frei and Polat (2007) reported a positive relationship between the $\varepsilon_{Nd}(i)$ and the iron content. Those authors found two distinct $\varepsilon_{Nd}(i)$ values corresponding to two interacting water masses: a Fe-rich end-member (magnetite-rich bands) with $\varepsilon_{Nd}(i)$ values of ∼+3.1 and a Fe poor end-member (silica-rich bands) with $\varepsilon_{Nd}(i)$ of ∼+1.2. In the 2.5 Ga Hamersley BIF, Jacobsen and Pimentel-Klose (1988) noted only positive $\varepsilon_{Nd}(i)$ values (0 to +4) and concluded that the REYs and Fe were derived from depleted hydrothermal fluids from a MORB-type setting.

$\varepsilon_{Nd}(i)$ values for the Itilliarsuk BIF and the contemporaneous Pongola BIF and Nemo BIF from South Dakota (all 2.9 Ga) are displayed in Fig. 17. The Pongola BIF records consistently negative $\varepsilon_{Nd}(i)$ values. By obtaining equivalent negative $\varepsilon_{Nd}(i)$ values for interbedded shales in the Pongola BIF succession (the inserted range bar in Fig. 17), Alexander et al. (2008) concluded that the REY content in the BIF was dominated by solutes from weathering of the adjacent enriched continental crust. Likewise, general negative $\varepsilon_{Nd}(i)$ values for the 2.9 Ga Nemo BIF were attributed to continental enriched crust as the dominant REY source (Frei et al., 2008). In contrast, the associated lithologies to the Itilliarsuk BIF have all positive $\varepsilon_{Nd}(i)$, ranging from +1.19 to +4.07 (the inserted range bar in Fig. 17). Hence, the negative $\varepsilon_{Nd}(i)$ values for the Fe-rich bands, and the general very low positive $\varepsilon_{Nd}(i)$ values for the silica-rich mesobands in sample 514935, imply that the REYs cannot be controlled solely by the associated lithologies.

Assuming that the source for the iron is the same as the source responsible for the negative $\varepsilon_{Nd}(i)$ values in the Itilliarsuk BIF, the following possible interpretations can be made: (1) submarine hydrothermal fluids interacted with an enriched mafic crust and thereby inherited low $^{143}Nd/^{144}Nd$-values and mobilised Fe(II); and (2) subaerial weathering of an enriched mafic continental crust exposed in the hinterland. The LREE-enriched metagabbroic sill (sample 514907) has $\varepsilon_{Nd}(i)$ value of +2.94, and is such enriched relative to the depleted mantle model. This could verify possible weak interaction with an unusual enriched mantle reservoir (?). On the other hand, the gabbros presumably intruded through the sialic TTG-basement with $\varepsilon_{Nd}(i)$ of +1.19, which suggest crustal contamination as the cause for the $\varepsilon_{Nd}(i)$ value of +2.94. Metagabbros with negative $\varepsilon_{Nd}(i)$ values have been reported by Schiøtte (1988) further north in the Rinkian fold belt, suggesting interaction with an enriched continental crust. Similarly, the 2.7 Ga metagabbroic complex from the Abitibi Greenstone belt showed weak interaction with enriched crust making Bleeker (2002) to conclude that the underlying orthogneiss domain was linked to the above greenstone belt during volcanic activity.

6.4. The depositional basin of the Itilliarsuk BIF

6.4.1. The significance of the BIF

The alternating, distinct magnetite- and silica-rich bands in sample 514935 reflect stable basinal conditions during precipitation and deposition of the Itilliarsuk BIF. Disturbing factors such as wave action, changes in seawater level, submarine debris flows, tectonic activity etc. were minor during BIF deposition. The palaeo-depth must as a minimum has been below storm-wave base, some 200 m, which is the average depth of the modern storm-wave base (Klein, 2005). Most of the minerals in the Itilliarsuk BIF are of secondary origin, so little can be deduced from the original primary phases that precipitated. However, the occurrence of magnetite as the main Fe-phase suggests that the redox level of the seawater permitted nearly continuous precipitation of ferric oxyhyroxides. Since the water column most likely was anoxic, the most sensible Fe(II) oxidizing mechanism could have been anoxygenic Fe(II)
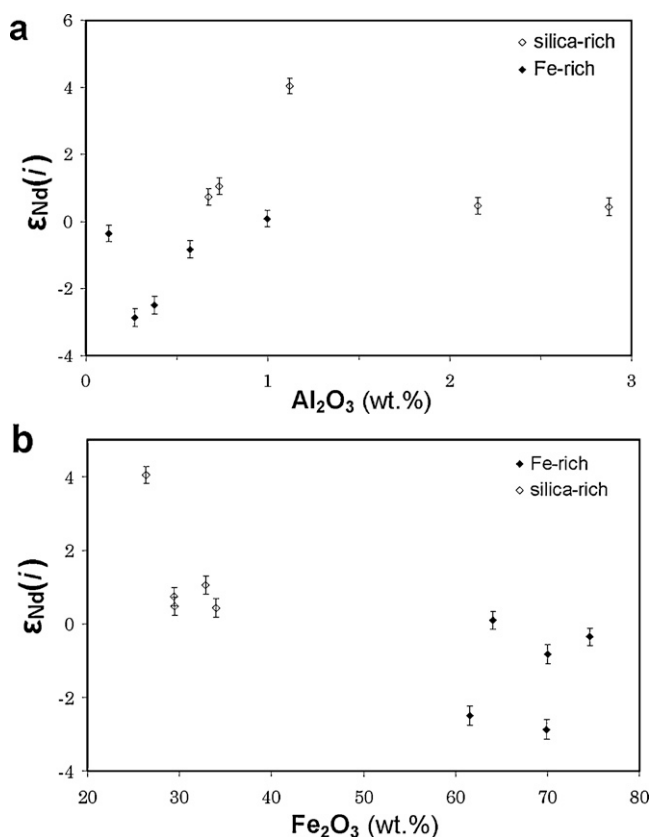
Fig. 16. The relationship between (a) the initial ε_{Nd} and Al and (b) the initial ε_{Nd} and Fe for the five silica-rich and five iron-rich bands from sample 514935. The fact that the lowest and negative $\varepsilon_{Nd}(i)$ values are found in the iron-rich bands, and generally, the highest alumina-content appear in the depleted silica-rich bands contrasts the general consensus regarding the sources of world BIFs (see Section 6.3.2). Error bars for $\varepsilon_{Nd}(i)$ are calculated assuming average errors of 0.5% on the $^{147}Sm/^{144}Nd$ ratios.
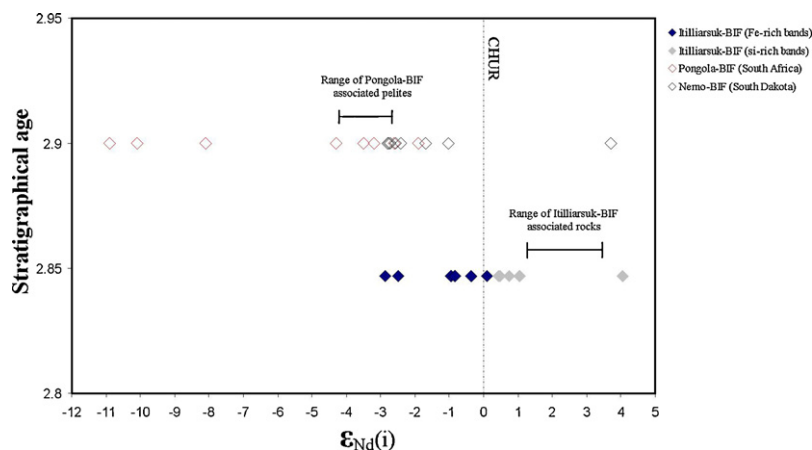
Fig. 17. Initial $\varepsilon_{Nd}(i)$ values between the Itilliarsuk BIF and the approximately same age (oxide-facies) Pongola BIF (South Africa) and Nemo BIF (South Dakota). The Itilliarsuk BIF is represented by the chemically pure sample 514935. By measuring enriched $\varepsilon_{Nd}(i)$ values (inserted range bar) in associated pelites of the Pongola BIF made Alexander et al. (2008) to suggest that erosion of the adjacent continental crust controlled the REY in the Pongola BIF. The same REY control was reported by Frei et al. (2008) for the Nemo BIF. In the same manner as for the Pongola BIF, the $\varepsilon_{Nd}(i)$ range bar is inserted for the associated lithologies analysed in the present study. As seen, none of these positive $\varepsilon_{Nd}(i)$ values can have played a major role in controlling the REY to the Fe-rich bands in the Itilliarsuk BIF. CHUR = Chondritic Uniform Reservoir. The Nemo BIF data from Frei et al. (2008) and the Pongola BIF data from Alexander et al. (2008). See Section 6.3.2 for further details.

oxidation by purple and/or green bacteria (as per Kappler et al., 2005).

Furthermore, if the existences of the faintly concordant layers of carbonate (presumably a calcite component, Fig. 7C) are of primary origin, it also indicates stages of supersaturation of carbonate in the palaeobasin, which only could have happened above the Archaean carbonate compensation depth (CCD). This depth is unknown but due to higher ρCO_2 in the atmosphere the compensation depth for calcite must have been shallower in Archaean time (Kramers, 2002).

Relatively high amount of detrital components in the shaley-BIF layers found in the lower part of the BIF zone excludes an abyssal plain deposit because of the expected rare influx of allochtonous detritus at these surroundings. A depositional site more proximal to the palaeo shoreline, possible on the shelf slope or even at the shelf, is more likely. Even though the Itilliarsuk BIF shows high variations in terrigenous influx between the lower part and central/upper part of the BIF zone, internal fluctuations in this influx are found within sample 514902 as well. The most clear seawater signature is contained in the mesoband 514902H. The PAAS-normalised REY pattern for this band shows HREE-enrichment analogous to the chemical pure Isua BIF (Frei and Polat, 2007) and the Penge BIF (Bau et al., 1997). This internal transition in sample 514902 from the seven mesobands A–G that contain high but variable content of the immobile elements to the chemically pure mesoband H reflects an unstable depositional system with cessation in the transport of terrigenous materials. These variations in clastic input could either be forced by tectonic processes, sea level changes, or processes related to the fluvial regime draining the hinterland.

6.4.2. The significance of the metasediments

To constrain the Itilliarsuk BIF depositional basin it is essential to identify the protoliths of the various types of schists exposed at Itilliarsuup Qaqqaa. The high modal content of ferro- and aluminium-rich minerals (especially staurolite), high concentrations of Al, Zr, Cr, and Ni, and the appearance of graphite (Fig. 8D) collectively suggest that the garnet–biotite schist and the staurolite schist are truly metapelites, hence, clay-rich sediments. The faintly laminated, fine-grained quartz–biotite–garnet schists are presumable meta-semipelites, with higher modal quartz, less Zr and less ferro- and aluminium-rich minerals than the metapelites. Furthermore, the unaltered plagioclase found in the meta-semipelites and the metapelites (e.g. Fig. 8A) probably indicates that the original

sediment was fine-grained clay with low permeability, thereby inhibiting the mobility of metasomatic fluids.

The nature of the felsic schists is of special interest in that they are syndepositional with the dense part of the BIF zone. No current-generated structures or well-defined laminae were observed in the field (in contrast to the meta-semipelites). Petrographical indications, such as the high content of poorly sorted, angular quartz grains, the absence of well-defined bedding, and the randomly distributed mica-flakes, tabular epidote and chlorite (Fig. 7D–F) all point towards the felsic schist being an immature felsic metagreywacke, most likely a first-cycle sediment (e.g., McLennan, 1984; Selley, 1988; Hegde and Chavadi, 2009). Moreover, the high amounts of poor-sorted, fine- to medium-grained angular quartz (Fig. 7E and F) indicate both short transport from the source to the depositional site, and that the flow process responsible for transporting the sediments were matrix-supported debris flows, as oppose to turbidite currents, which would prevent any particularly sorting or grading (e.g., Selley, 1988). A source proximal to the Itilliarsuk BIF basin is therefore favoured due to the general immaturity and the very poor sorting of the felsic metagreywackes.

The HREE patterns in Fig. 11 also show that the felsic metagreywackes are mixtures of material derived primarily either from the TTG-basement or felsic volcanic equivalents, with minor mafic material. However, we prefer that the source responsible for the angular quartz grains in the metagreywackes was felsic volcanics rather than subaerial weathering of a TTG-basement because the Sm–Nd isotope diagram in Fig. 15 excludes a dominant contribution from the TTG-basement to the felsic metagreywackes. It is generally accepted that Al and Ti do not fractionate during weathering, transportation and deposition (e.g., Sugitani et al., 1996, 2006) hence, the constant Al_2O_3/TiO_2 ratio of $\sim$40 for the felsic metagreywackes seems to be unlikely if the dominant felsic component was sourced from the TTG-plutonic basement with an Al_2O_3/TiO_2 ratio of 89. Furthermore, at Itilliarsuup Qaqqaa there is evidence of major felsic volcanics in close relation to the Itilliarsuk BIF (e.g., the sericite schist (Fig. 8B) and the younger acidic metavolcanic). The textural mature (well-rounded) quartz clasts seem to deviate from the predominantly textural immaturity. Three possible explanations can be addressed: (1) that the sialic basement contributed minor to the greywackes by derivation of highly textural mature grains; (2) the clasts represent recycled material from older quartz-rich sediment; (3) the clasts were original carbonate which, post to deposition, have been dissolved and subsequently cavity-filled with chert.

In contrast to more sorted and normal graded (fining upward) turbidite sequences, which are believed to have been deposited in a deep marine (abyssal plain) setting (e.g. Pickard et al., 2004), the alternating metagreywacke–BIF sequences were presumably deposited in a continental shelf or slope type setting within the basin. One possible explanation for the generation of the greywackes at the Itilliarsuup Qaqqaa would then be from erosion of active felsic volcanics that formed topographic highs within the basin from which rapidly, progressive sheets or flow-masses intermixed with BIF deposition on the marine platform. The accumulation of the felsic greywackes must have taken place below storm-wave base where wave action and wave-generated currents would have been unable to separate the clay from the sand-sized particles. It is also probable that the deposition may have taken place during regressive phases, which lowered the overall base level and thus prevented BIF deposition. Then, during transgressive conditions the Fe(II)-rich bottom waters could interact with the upper seawater zone, promoting BIF deposition.

The felsic metagreywackes, therefore, resemble a high-energy basin environment, where the deposition of individually units was rapid and sudden. In contrast, BIF is believed to represent longer time scale deposition. First order calculations from the 2.5 Ga BIF from the Hamersley Group, that were deposited as chemical varves in a continental shelf environment, yield (compacted) deposition rates between 20 and 225 m/Ma (Trendall and Blockley, 2004).

Opposed to the felsic metagreywackes, the meta-semipelite and, especially, the metapelites have (1) higher concentrations of MgO, Fe_2O_3, Cr, Ni, and V, (2) lower SiO_2 content, (3) lower Al_2O_3/TiO_2 ratios, and (4) are more HREE enriched – all are a consequence of higher contribution from mafic sources to the basin. In general, the metasediments at Itilliarsuup Qaqqaa show REE patterns that are consistent with "bimodal igneous-suites" comprising most of the Archaean crust (Taylor and McLennan, 1985, 1995). The gradational change in the type of metasediment (upwards in stratigraphy, see Fig. 2B) from metapelites to meta-semipelites to felsic metagreywackes reflects changes in the overall source terrain and depositional environment. Within the BIF zone, the meta-semipelites and the ferruginous shales reflect influx of fine-grained siliciclastic material to the depositional basin, which mixes with the BIF precipitation and eventually formed the shaley-BIF of mixed terrigenous and chemical sedimentary parentage. The evidence from the Nd isotopes reveals that during deposition of the most pure mesobands the REY in the basin were controlled by contributions from the TTG-basement and an unknown enriched mantle source; the latter responsible for the source of Fe(II) to the basin. During more unstable conditions within the Itilliarsuk BIF basin the overall REYs were controlled by erosion of bimodal felsic volcanics and mafic precursors, as seen in the Nd-signatures for the felsic metagreywackes, the sericite schist and the metapelites with higher positive $\varepsilon_{Nd}(i)$ values and T_{DM} ages only slightly older than the acidic metavolcanic (2847 ± 4 Ma).

Any direct link from mafic lithologies to the BIF formation is not evident in the field (e.g., pillow lavas). The adjacent southern metagabbro intruded the BIF, and thus, was not of any influence (Fig. 6B). However, the thin amphibole layers found concordant within the BIF (Fig. 6A) may represent some syndepositional mafic tuffs, which would indicate that mafic volcanism was active at some stage during the deposition of the Itilliarsuk BIF. Appel (1977) discovered similar thin amphibole layers interbedded within the 3.7 Ga Isua BIF, and interpreted them as being derived from submarine basaltic ash. Alternatively, and due to the fact that the Itilliarsuk BIF contains various amount of detritus, the protolith of these layers could also represents marly sediment with clay- and carbonate-rich material.

6.5. The palaeo-tectonic setting

The Itilliarsuk BIF belongs to a supracrustal succession in a possible greenstone belt environment which rest on a TTG-basement. The metasediments reflect a transition between mafic dominated metapelites to more felsic dominated metagreywackes, while the BIF presumably resulted from major changes in the tectonic regime, from tectonic stable periods (BIF deposition) to tectonic unstable periods (greywacke deposition). The generally accepted model for the origin of TTG-suites involves subduction of an oceanic plate, where slab melting and slab dehydration of warm mafic oceanic crust generates TTG melts in equilibrium with a garnet-clinopyroxene ± amphibole residue (Taylor and McLennan, 1995; Martin et al., 2005; Rollinson, 2007). Melt extraction in the garnet stability field would explain the geochemical characteristics of the TTG-basement at Itilliarsuup Qaqqa (highly fractionated REE pattern, low concentrations of transition metals, absence of Eu-anomaly and high concentration of strontium – as a result of the absence of plagioclase in the source).

The Th–Sc–Zr and La–Th–Sc ternary tectonic discrimination plots for Archaean metasediments have been used by various workers to infer tectonic settings (e.g. Bhatia and Crook, 1986; Toulkeredis et al., 1999). The Itilliarsuup Qaqqaa metasediments are plotted in these diagrams in Fig. 18. In both diagrams the felsic metagreywackes, the meta-semipelites and the metapelites all plot within, or close, to the ocean island arc (OIA) field. This contrasts with the continental island arc (CIA) setting suggested by Rasmussen and Pedersen (1999) for quartz–biotite schists of Naajaat Qaqqaat immediately west of Itilliarsuup Qaaqaa (Fig. 1). Those authors utilised tectonic discrimination diagrams involving major elements such as Fe_2O_3, MgO, CaO, Na_2O and K_2O. Due to the
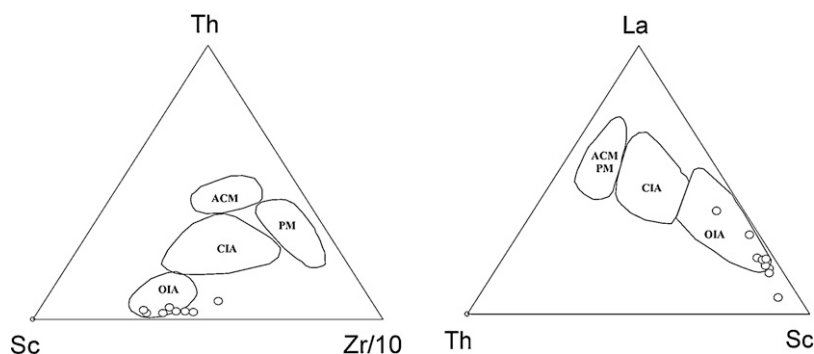

Fig. 18. Th–Sc–Zr and La–Th–Sc discrimination diagrams plotting the metasediments at Itilliarsuup Qaqqaa into the tectonic regime. ACM = active continental margin; PM = passive margin; CIA = continental island arc; OIA = ocean island arc. The data points represent the metagreywackes, meta-semipelites and metapelites. The samples plot within or close to the ocean island arc field suggesting that the sediments were derived from an island arc.
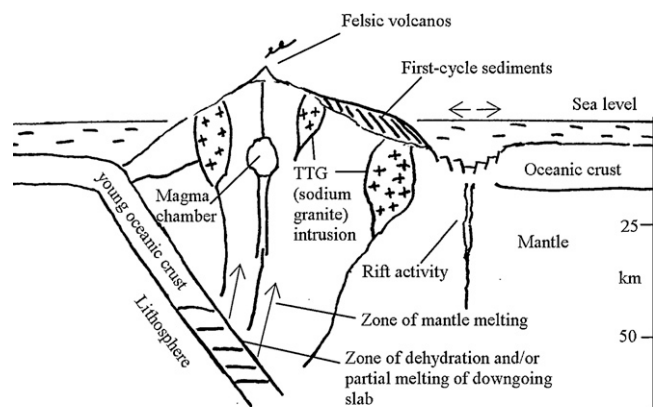
Fig. 19. Shows a possible Archaean tectonic setting for the TTG-basement and the supracrustals at Itilliarsuup Qaqqaa. The TTG-igneous suites are generated through dehydration and/or melting in the garnet stability field of the young subducted oceanic crust. The Itilliarsuk BIF was deposited in a basin related to hydrothermal rift activity, and deposition of first-cycle sediments that were shed from the adjacent juvenile arc. Modified after Windley (1984) and Taylor and McLennan (1995). The metagabbroic sills may have intruded the sequence later during further rifting.

relatively high-grade metamorphism in the area we prefer to apply less mobile elements to characterise the overall tectonic regime.

The role of the metagabbroic sills in the overall depositional and tectonic regime is unclear. These sills are characterised by coarse-to very coarse-grained textures and have experienced moderate to high alteration by secondary silica-rich fluids. The very low ΣREE of these samples contrasts with the higher REE concentrations of the Naajaat Qaqqaat amphibolites (Rasmussen and Pedersen, 1999). The low ΣREE, the relative low plagioclase content, and the texture shown in Fig. 8E–G suggest that their protoliths may have been pyroxene-rich cumulates, where incompatible trace elements were concentrated in the inter-cumulus melt. In this regard, it is preferable to use ratios of elements with comparable chemical behaviour, when applying tectonic discrimination diagrams to these rocks. Ti and V are both elements with high ionic potential and same chemical behaviour during partial melting of the mantle source and are compatible in the same phases (Rollinson, 1993). This is consistent with the strong correlation observed between these elements in the metagabbros ($R = 0.998$). According to Condie (1989) arc-tholeiites generally have low Ti/V ratios (<30), whereas within-plate basalts generally have higher ratios (>30). The metagabbros from this study have fairly constant Ti/V ratios of ~20, which suggest an origin as arc-tholeiites.

A general sketch of a possible tectonic setting for the origin of the Itilliarsuk BIF and the associated rocks is displayed in Fig. 19. We propose that the Itilliarsuk BIF was deposited in a back-arc or intra-arc basin related to an ocean island arc (OIA) setting. Submarine hydrothermal activity in the basin contributed to the Itilliarsuk BIF. The immature (first-cycle) volcanic–sedimentary deposits within the basin were shed from the adjacent magmatic arc (e.g. Taylor and McLennan, 1995; Veizer and Mackenzie, 2003). The above island arc scenario has also been reported for other greenstone belts containing BIF (e.g. the ~2.7 Ga Slave craton, Canada (Bleeker, 2002), the Kaapvaal craton in South Africa and the Pilbara craton in West Australia (Kusky and Polat, 1999)).

7. Conclusions

The ~2.5 km thick supracrustal succession at Itilliarsuup Qaqqaa reflects transition from mafic dominated metapelites, to meta-semipelites and a more felsic dominated regime as recorded by the metagreywackes, to the acidic metavolcanic terminating

the sequence. The Itilliarsuk BIF is found interbedded with felsic metagreywackes, meta-semipelites and ferruginous shales. Metagabbroic sills, found in the lower and upper part of the sequence, are interpreted as arc-tholeiites. The uppermost sill intrudes the BIF precluding any contribution from this body in the genesis of the Itilliarsuk BIF.

The supracrustals have undergone amphibolite-facies metamorphism, which led to resetting of the uranium-lead system at an apparent age of 1848 ± 48 Ma. This tectono-metamorphic event corresponds to the Rinkian orogeny known from this region. The Itilliarsuk BIF has been divided into two units: a shaley-BIF unit and a more mineralogic and chemically pure BIF. The shaley-BIF is composed of mesobands with mixture of chemical and terrigenous components. This is reflected in both the geochemistry (high Al_2O_3, HFSE and the transition metals) and the appearance of biotite, hornblende, epidote, and occasionally garnets. The chemically pure BIF contains micro- and mesobands, which reflect chemical precipitation during stable water conditions (low detritus, distinct silica- and Fe-rich bands, and a more pronounced shale-normalised HREE-enrichment relative to LREE). Distinct seawater-derived La/La* and hydrothermal-derived Eu/Eu*-anomalies characterise the Itilliarsuk BIF. Many of the BIF samples record positive Ce/Ce*-values, presumably due to mobilisation of Ce(IV) during secondary alteration. In line with this, and in agreement with world-wide Archaean BIFs, the least altered mesobands do not exhibit cerium-anomalies which point towards low O_2-conditions in the water column where Fe(II) was oxidised and hydrolysed to ferric oxyhydroxides during BIF deposition. Fractionation of Y relative to Ho is not seen for the Itilliarsuk BIF, although two layers do exhibit a seawater signal (Y/Ho > 30). Suppression of this ratio by continental crustal material and/or hydrothermal-derived fluids exhibiting chondritic uniform Y/Ho ratio of ~26, is considered most likely. Support for influx of submarine hydrothermal fluids to the system is reflected by a general enrichment of MREE relative to both LREE and HREE. A lack of correlation between the REY and Al_2O_3, HFSE and transition elements suggest that part of the REY came to the depositional site as solutes and was not deposited with the clay-rich fraction. Mixing of REY from different sources is supported by Sm–Nd isotope systematics. The chemically pure BIF shows systematic variations between silica-rich bands with average positive $\varepsilon_{Nd}(i)$ values of +1.35, and iron-rich bands with average, negative $\varepsilon_{Nd}(i)$ values of −1.29. These data contrast sharply with BIF elsewhere, where the Fe is believed to has been sourced from hydrothermal alteration of oceanic crust with depleted, positive $\varepsilon_{Nd}(i)$ values, whereas those with negative $\varepsilon_{Nd}(i)$ values came from erosion of enriched, continental crustal sources (e.g. Jacobsen and Pimentel-Klose, 1988; Frei and Polat, 2007; Alexander et al., 2008; Alexander et al., 2009). Highest content of Al_2O_3 in the silica-rich bands further documents that the silica and the REYs in shallower seawater were derived from the nearby landmasses, exhibiting positive $\varepsilon_{Nd}(i)$ values. This scenario might also explain the generally low trace metal concentrations (e.g., Ni) in the BIF; while high Ni in other BIF was likely sourced from ultramafic volcanic rocks (e.g., komatiites), the Itilliarsuk BIF was influenced by bimodal volcanism of mafic (e.g., tholeiites) and felsic (e.g., dacites–rhyolites) sources which would have diluted the local water column of Ni.

None of the associated rocks at Itilliarsuup Qaqqaa are responsible for the negative $\varepsilon_{Nd}(i)$ values found in the Itilliarsuk BIF. On a Sm–Nd isochron diagram these low and negative $\varepsilon_{Nd}(i)$ values suggest control of REY during stable basinal conditions by mixing between a felsic TTG-basement component with $\varepsilon_{Nd}(i)$ of +1.19, and an older, now unexposed, enriched source. Hydrothermal fluids sourced from the latter reservoir were responsible for the MREE enrichment and the input of Fe(II) to the Itilliarsuk BIF depositional basin. In contrast, the shaley-BIF and the associated rocks at Itilliarsuup Qaqqaa all have comparable T_{DM} ages and positive $\varepsilon_{Nd}(i)$

values, which suggests an overall control on REY by input from juvenile felsic and mafic crustal sources.

The Itilliarsuk BIF basin shifted between stable periods of BIF deposition and dynamic periods with deposition of volcanogenic dominated greywackes and fine-grained epiclastic sediments (semipelites and ferruginous shales). The intercalated felsic metagreywackes and the often high input of terrigenous material in the BIF, indicates that the Itilliarsuk BIF was deposited in a continental slope or shelf-type environment rather than on the abyssal plain. Utilising Th–Sc–Zr and La–Th–Sc tectonic discrimination plots of the metasediments at Itilliarsuup Qaqqaa indicates that the tectonic regime for the supracrustal package has been an ocean island arc-setting where the Itilliarsuk BIF was deposited in a basin related to back-arc or intra-arc extension.

Acknowledgements

References

Alexander, B.W., Bau, M., Andersson, P., Dulski, P., 2008. Continentally-derived solutes in shallow Archean seawater: rare earth element and Nd isotope evidence in iron formation from the 2.9 Ga Pongola Supergroup, South Africa. Geochimica et Cosmochimica Acta 72, 378–394.

Alexander, B.W., Bau, M., Andersson, P., 2009. Neodymium isotopes in Archean seawater and implications for the marine Nd cycle in Earth's early oceans. Earth and Planetary Science Letters 283, 144–155.

Anders, E., Grevesse, N., 1989. Abundances of the elements: meteoric and solar. Geochimica et Cosmochimica Acta 53, 197–214.

Appel, P.W.U., 1977. Aeolian differentiation of basaltic tuffs in the early Precambrian Isua supracrustal belt, West Greenland. Neues Jahrbuch fuer Mineralogie, Monatshefte, pp. 521–528.

Arndt, N.T., 1991. High Ni in Archean tholeiites. Tectonophysics 187, 411–420.

Arndt, N.T., Barnes, S.J., Lesher, C.M., 2008. Komatiite. Cambridge University Press, 488 pp.

Bau, M., 1993. Effects of syn- and post-depositional processes on the rare-earth element distribution in Precambrian iron-formations. European Journal of Mineralogy 5, 257–267.

Bau, M., Möller, P., 1993. Rare earth element systematics of the chemically precipitated component in Early Precambrian iron formations and the evolution of the terrestrial atmosphere-hydrosphere-lithosphere system. Geochimica et Cosmochimica Acta 57, 2239–2249.

Bau, M., Dulski, P., 1996. Distribution of yttrium and rare-earth elements in the Penge and Kuruman iron-formations, Transvaal Supergroup, South Africa. Precambrian Research 79, 37–55.

Bau, M., Höhndorf, A., Dulski, P., Beukes, N.J., 1997. Sources of rare earth elements and iron in Paleoproterozoic iron-formations from the Transvaal Supergroup, South Africa: evidence from neodymium isotopes. Journal of Geology 105, 121–129.

Bau, M., Dulski, P., 1999. Comparing yttrium and rare earths in hydrothermal fluids from the Mid-Atlantic Ridge: implications for Y and REE behaviour during nearvent mixing and for the Y/Ho ratio of Proterozoic seawater. Chemical Geology 155, 77–90.

Bekker, A., Slack, J.F., Planavsky, N., Krapež, B., Hofmann, A., Konhauser, K.O., Rouxel, O.J., 2010. Iron formation: the sedimentary product of a complex interplay among mantle, tectonic, oceanic, and biospheric processes. Economic Geology 105, 467–508.

Bhatia, R.M., Crook, A.W.K., 1986. Trace element characteristics of graywackes and tectonic setting discrimination of sedimentary basins. Contribution to Mineralogy and Petrology 92, 181–193.

Bleeker, W., 2002. Archean tectonics: a review, with illustrations from the Slave craton. In: Fowler, C.M.R., Ebinger, C.J., Hawkesworth, C.J. (Eds.), The Early Earth: Physical, Chemical and Biological Development, vol. 199. The Geological Society, London, pp. 151–181.

Bolhar, R., Kamber, B.S., Moorbath, S., Fedo, C.M., Whitehouse, M.J., 2004. Characterisation of early Archaean chemical sediments by trace element signatures. Earth and Planetary Science Letters 222, 43–60.

Bolhar, R., Kamber, B.S., Moorbath, S., Whitehouse, M.J., Collerson, K.D., 2005. Chemical characterization of earth's most ancient clastic metasediments from the Isua Greenstone Belt, southern West Greenland. Geochimica et Cosmochimica Acta 69, 1555–1573.

Condie, K.C., 1989. Geochemical changes in basalts and andesites across the Archaean-Proterozoic boundary: identification and significance. Lithos 23, 1–18.

Condie, K.C., 1997. Plate Tectonics and Crustal Evolution. Butterworth-Heinemann, Oxford, 282 pp.

Connelly, J.N., Thrane, K., Krawiec, A.W., Garde, A.A., 2006. Linking the Palaeoproterozoic Nagssugtoqidian and Rinkian orogens through the Disko Bugt region of West Greenland. Journal of the Geologocal Society, London 163, 319–335.

DePaolo, D.J., 1981. Neodymium isotopes in the Colorado Front Range and crustmantle evolution in the proterozoic. Nature 291, 193–196.

De Wit, M.J., Hart, R.A., 1993. Earth's earliest continental lithosphere, hydrothermal flux and crustal recycling. Lithos 30, 309–335.

Eigenbrode, J.L., Freeman, K.H., 2006. Late Archean rise of aerobic microbial ecosystems. Proceedings of the National Academy of Sciences of the United States of America 103, 15759–15764.

Eigenbrode, J.L., Freeman, K.H., Summons, R.E., 2008. Methylhopane biomarker hydrocarbons in Hamersley Province sediments provide evidence for Neoarchean aerobiosis. Earth and Planetary Science Letters 273, 323–331.

Frei, R., Polat, A., 2007. Source heterogeneity for the major components of ~3.7 Ga Banded Iron Formations (Isua Greenstone Belt, Western Greenland): tracing the nature of interacting water masses in BIF formation. Earth and Planetary Science Letters 253, 266–281.

Frei, R., Dahl, P.S., Duke, E.F., Frei, K.M., Hansen, T.R., Frandsson, M.M., Jensen, L.A., 2008. Trace element and isotopic characterization of Neoarchaean and Paleoproterozoic iron formations in the Black Hills (South Dakota, USA): assessment of chemical change during 2.9–1.9 Ga deposition bracketing the 2.4–2.2 Ga first rise of atmospheric oxygen. Precambrian Research 162, 441–474.

Frei, R., Gaucher, C., Poulton, S.W., Canfield, D.E., 2009. Fluctuations in Precambrian atmospheric oxygenation recorded by chromium isotopes. Nature 461, 250–253.

Garde, A.A., Steenfelt, A., 1999. Precambrian geology of Nuussuaq and the area northeast of Disko Bugt, West Greenland. In: Karlsbeek, F. (Ed.), Precambrian Geology of the Disko Bugt Region, West Greenland. Geology of Greenland Survey Bulletin, vol. 181, pp. 6–40.

Garde, A.A., Connelly, J.N., Krawiec, A.W., Piazolo, S., Thrane, K., 2002. A coastal survey in the southern part of the Palaeoproterozoic Rinkian fold belt, central West Greenland. Geology of Greenland Survey Bulletin 191, 33–38.

Godfrey, L.V., Falkowski, P.G., 2009. The cycling and redox state of nitrogen in the Archaean ocean. Nature Geoscience 2, 725–729.

Hamade, T., Konhauser, K.O., Raiswell, R., Goldsmith, S., Morris, R.C., 2003. Using Ge/Si ratios to decouple iron and silica fluxes in Precambrian banded iron formations. Geology 31, 35–38.

Hegde, V.S., Chavadi, V.S., 2009. Geochemistry of late Archean metagreywackes from the Western Dharwar Craton, South India: implications for provenance and nature of the Late Archean crust. Gondwana Research 15, 178–187.

Hofmann, A., 2005. The geochemistry of sedimentary rocks from the Fig Tree Group, Barbeton greenstone belt: implications for tetonic, hydrothermal and surface processes during mid-Archaean times. Precambrian Research 143, 23–49.

Jacobsen, B.S., Pimentel-Klose, R.M., 1988. A Nd isotopic study of the Hamersley and Michipicoten banded iron formations: the source of REE and Fe in Archean Oceans. Earth and Planetary Science Letters 87, 29–44.

Johannesson, K.H., Hawkins Jr., D.L., Cortés, A., 2006. Do Archean chemical sediments record ancient seawater rare earth element patterns? Geochimica et Cosmochimica Acta 70, 871–890.

Kamber, B.S., Whitehouse, M.J., Bolhar, R., Moorbath, S., 2005. Volcanic resurfacing and the early terrestrial crust: zircon U-Pb and REE constraints from the Isua Greenstone Belt, southern West Greenland. Earth and Planetary Science Letters 240, 276–290.

Kappler, A., Pasquero, C., Konhauser, K.O., Newman, D.K., 2005. Deposition of banded iron formations by anoxygenic phototrophic Fe(II)-oxidizing bacteria. Geology 33, 865–868.

Kendall, B., Reinhard, C.T., Lyons, T.W., Kaufman, A.J., Poulton, S.W., Anbar, A.D., 2010. Pervasive oxygenation along late Archaean ocean margins. Nature Geoscience 3, 647–652.

Khan, R.M.K., Naqvi, S.M., 1995. Geology, geochemistry and genesis of BIF of Kushtagi schist belt, Archaean Dharwar Craton, India. Mineralium Deposita 31, 123–133.

Klein, C., 2005. Some Precambrian banded iron-formations (BIF's) from around the world: their age, geological setting, mineralogy, metamorphism, geochemistry, and origin. American Mineralogist 90, 1473–1499.

Konhauser, K.O., Pecoits, E., Lalonde, S.V., Papineau, D., Nisbet, E.G., Barley, M.B., Arndt, N.T., Zahnle, K., Kamber, B.S., 2009. Oceanic nickel depletion and a methanogen famine before the Great Oxidation Event. Nature 458, 750–754.

Konhauser, K.O., Lalonde, S.V., Planavsky, N.J., Pecoits, E., Lyons, T.W., Mojzsis, S.J., Rouxel, O.J., Barley, M.E., Rosìere, C., Fralick, P.W., Kump, L.R., Bekker, A., 2011. Aerobic bacterial pyrite oxidation and acid rock drainage during the Great Oxidation Event. Nature 478, 369–373.

Kramers, J.D., 2002. Global maodelling of continent formation and destruction through geological time and implications for CO₂ drawdown in the Archaean Eon. In: Fowler, C.M.R., Ebinger, C.J., Hawkesworth, C.J. (Eds.), The Early Earth:

Physical, Chemical and Biological Development, vol. 199. The Geological Society, London, pp. 259–274.

Ludwig, K.R., 2005. Users's Manual for Isoplot 3.00: A Geochronological Toolkit for Microsoft Excel. Berkely Geochronology Center, 70 pp.

Kusky, T.M., Polat, A., 1999. Growth of granite-greenstone terranes at convergent margins, and stabilization of Archean cratons. Techtonophysics 305, 43–73.

Martin, H., Smithies, R.H., Rapp, R., Moyen, J.-F., Champion, D., 2005. An overview of adakite, tonalite-trondhjemite-granodiorite (TTG), and sanukitoid: relationships and some implications for crustal evolution. Lithos 79, 1–24.

McLennan, S.M., 1984. Petrological characteristics of Archean graywackes. Journal of Sedimentary Petrology 54, 889–898.

Nutman, A.P., 1986. The early Archaean to proterozoic history of the Isukasia area, southern West Greenland. The Geological Survey of Greenland bulletin 154, 80.

Nutman, A.P., Fryer, B.J., Bridgewater, D., 1989. The early Archaean Nulliak (supracrustal) assemblage, northern Labrador. Canadian Journal of Earth Science 26, 2159–2168.

Petersen, J.S., 1997. Gold exploration in the Saqqaq, Itilliarsuup, Eqe and Christianshaab areas. Nunaoil field report, 26 pp.

Pickard, A.L., Barley, M.E., Krapez, B., 2004. Deep-marine depositional setting of banded iron formation: sedimentological evidence from interbedded clastic sedimentary rocks in the early Pa-laeoproterozoic Dales George Member of Western Australia. Sedimentary Geology 170, 37–62.

Polat, A., Frei, R., Appel, P.W.U., Dilek, Y., Fryer, B., Ordóñez-Calderón, J.C., Yang, Z., 2008. The origin and compositions of Mesoarchean oceanic crust: evidence from the 3075 Ma Ivisaartoq greenstone belt, SW Greenland. Lithos 100, 293–321.

Rasmussen, H., Holm, P.M., 1999. Proterozoic thermal activity in the Archaean basement of the Disko Bugt region and eastern Nuussuaq, West Greenland: evidence from K-Ar and 40Ar-39Ar mineral age investigations. In: Karlsbeek, F. (Ed.), Precambrian Geology of the Disko Bugt Region, West Greenland. Geology of Greenland Survey Bulletin, vol. 181, pp. 55–64.

Rasmussen, H., Pedersen, L.F., 1999. Stratigraphy, structure and geochemistry of Archaean supracrustal rocks from Oqaatsut and Naajaat Qaqqaat, north-east Disko Bugt, West Greenland. In: Karlsbeek, F. (Ed.), Precambrian Geology of the Disko Bugt Region. Geology of Greenland Survey Bulletin, vol. 181, pp. 65–78.

Rollinson, H.R., 1983. The geochemistry of mafic and ultramafic rocks from the Archaean green-stone belts of Sierra Leone. The Mineralogical Magazine, the Mineralogical Society 47, 267–280.

Rollinson, H., 1993. Using geochemical data: evaluation, presentation, interpretation. Longman Group, UK, 352 pp.

Rollinson, H., 2007. Early Earth System – A Geochemical Approach. Blackwell Publishing, 285 pp.

Rosing, M.T., Frei, R., 2004. U-rich Archaean sea-floor sediments from Greenland – indications of >3700 Ma oxygenic photosynthesis. Earth and Planetary Science Letters 217, 237–244.

Schiøtte, L., 1988. Field occurrence and petrology of deformed metabasite bodies in the Rinkian mobile belt, Umanak district, West Greenland. Rapport Grønlands Geologiske Undersøgelse 141, 36.

Selley, R.C., 1988. Applied Sedimentology. Academic Press, 446 pp.

Stacey, J.S., Kramers, J.D., 1975. Approximation of terrestrial lead isotope evolution by a two-stage model. Earth and Planetary Science Letters 26, 207–221.

Steinhöfel, G., von Blanckenburg, F., Horn, I., Konhauser, K.O., Beukes, N.J., Gutzmer, J., 2010. Deciphering formation processes of banded iron formations from the Transvaal and the Hamersley successions by combined Si and Fe isotope analysis using UV femtosecond laser ablation. Geochimica et Cosmochimica Acta 74, 2677–2696.

Sugitani, K., Horiuchi, Y., Adachi, M., Sugisaki, R., 1996. Anomalously low Al_2O_3/TiO_2 values for Archean cherts from the Pilbara Block, Western Australia-possible evidence for extensive chemical weathering on the early earth. Precambrian Research 80, 49–76.

Sugitani, K., Yamashita, F., Nagaoka, T., Yamamoto, K., Minami, M., Mimura, K., Suzuki, K., 2006. Geochemistry and sedimentary petrology of Archean clastic sedimentary rocks at Mt. Goldsworthy, Pilbara Craton, Western Australia: evidence for the early evolution of continental crust and hydrothermal alteration. Precambrian Research 147, 124–147.

Taylor, S.R., McLennan, S.M., 1985. The Continental Crust: Its Composition and Evolution. Blackwell Scientific, Oxford, 312 pp.

Taylor, S.R., McLennan, S.M., 1995. The geochemical evolution of the continental crust. Reviews of Geophysics 33, 241–265.

Toulkeredis, T., Clauer, N., Kröner, A., Reimer, T., Todt, W., 1999. Characterization, prove-nance, and tectonic setting of Fig Tree greywackes from the Archaean Barbeton Greenstone Belt, South Africa. Sedimentary Geology 124, 113–129.

Trendall, A.F., Blockley, J.G., 2004. Precambrian iron-formation. In: Eriksson, P.G., Altermann, W., Nelson, D.R., Mueller, W.U., Catuneanu, O. (Eds.), The Precambrian Earth: Tempos and Events. Developments in Precambrian Geology, vol. 12. Elsevier, Amsterdam, pp. 403–421.

Veizer, J., Mackenzie, F.T., 2003. Evolution of sedimentary rocks. Treatise on Geochemistry, vol. 7. Elsevier, Amsterdam, pp. 369–407.

Wang, Z., Wilde, S.A., Wang, K., Yu, L., 2004. A MORB-arc basalt-adakite association in the 2.5 Ga Wutai greenstone belt: late Archean magmatism and crustal growth in the North China Craton. Precambrian Research 131, 323–343.

Windley, B.F., 1984. The Evolving Continents. John Wiley and Sons Limited, 399 pp.